

1 Selective autophagic clearance of protein aggregates is mediated by the autophagy receptor,
2 TAX1BP1

3 Shireen A. Sarraf¹, Hetal V. Shah^{1,2}, Gil Kanfer¹, Michael E. Ward¹, Richard J. Youle^{1,2}

4 ¹ Biochemistry Section, Surgical Neurology Branch, National Institute of Neurological Disorders
5 and Stroke, National Institutes of Health, Bethesda, MD 20892, USA

6 ² Program in Neuroscience & Cognitive Science, University of Maryland, College Park,
7 Maryland, USA

8 *Corresponding author: youler@ninds.nih.gov

9 **Abstract**

10 Misfolded protein aggregates can disrupt cellular homeostasis and cause toxicity, a
11 hallmark of numerous neurodegenerative diseases. Protein quality control by the ubiquitin
12 proteasome system (UPS) and autophagy is vital for clearance of aggregates and maintenance of
13 cellular homeostasis¹. Autophagy receptor proteins bridge the interaction between ubiquitinated
14 proteins and the autophagy machinery allowing selective elimination of cargo². Aggrephagy is
15 critical to protein quality control, but how aggregates are recognized and targeted for degradation
16 is not well understood. Here we examine the requirements for 5 autophagy receptor proteins:
17 OPTN, NBR1, p62, NDP52, and TAX1BP1 in proteotoxic stress-induced aggregate clearance.
18 Endogenous TAX1BP1 is both recruited to and required for the clearance of stress-induced
19 aggregates while overexpression of TAX1BP1 increases aggregate clearance through autophagy.
20 Furthermore, TAX1BP1 depletion sensitizes cells to proteotoxic stress and Huntington's disease-
21 linked polyQ proteins, whereas TAX1BP1 overexpression clears cells of polyQ protein
22 aggregates by autophagy. We propose a broad role for TAX1BP1 in the clearance of cytotoxic
23 proteins, thus identifying a new mode of clearance of protein inclusions.

24 **Main**

25 Maintenance of cellular and organismal health is intricately connected to protein quality
26 control. A balance exists between protein translation, folding, and degradation that maintains the
27 stoichiometry and function of cellular protein complexes and organelles. If this balance is
28 perturbed, the accumulation of misfolded proteins can be toxic to the cell and is associated with
29 disruption of cellular function and numerous neurodegenerative diseases such as amyotrophic
30 lateral sclerosis (ALS), Huntington's disease (HD), and Alzheimer's disease (AD)³. A number of
31 protein quality control pathways exist within the cell to forestall dysfunction. Molecular
32 chaperone systems function to monitor and refold proteins if possible, while misfolded or

33 damaged proteins are targeted for elimination via autophagy or the UPS^{4,5}. The UPS is generally
34 responsible for routine turnover of short-lived proteins and targeted degradation of soluble or
35 solubilized misfolded proteins while macroautophagy, a catabolic process, culminates in the
36 lysosomal degradation of long-lived proteins, damaged organelles, and portions of the
37 cytoplasm⁶⁻⁹. Since the proteasome can only accommodate unfolded polypeptide chains, it is
38 generally thought that autophagy is responsible for the removal of insoluble protein
39 aggregates^{1,10}. If either autophagy or the UPS is hindered, acute or chronic proteotoxic stress,
40 such as that caused by the expression of mutated proteins in neurodegenerative disease, can
41 result in the selective accumulation of these aggregation-prone proteins¹¹⁻¹³. *In vivo*, inhibition of
42 autophagy results in intracellular protein aggregation contributing to neuronal cell death and
43 neurodegeneration in mice^{14,15}.

44 In recent years, numerous studies have highlighted the ability of autophagy to selectively
45 eliminate specific substrates, including mature ribosomes, endoplasmic reticulum, intracellular
46 pathogens, mitochondria, and protein aggregates¹⁶⁻¹⁹. In these cases, the autophagic machinery
47 employed in nonselective bulk degradation of cytosolic material is targeted to specific cargo.
48 Stimulation of autophagy is a promising therapeutic strategy in the treatment of protein
49 aggregation diseases and has been shown to enhance turnover of aggregated proteins, such as
50 TDP-43, in neuronal ALS models and huntingtin protein in Huntington disease models²⁰⁻²². Key
51 to this approach is an understanding of how autophagy is selectively targeted to aggregates. In
52 addition to the specificity mediated by E3 ubiquitin (UB) ligases that target their cognate
53 substrates, there is selectivity in delivery to the proteasome via UB receptors²³ and in the
54 recruitment of autophagic machinery via autophagy receptors which associate with
55 polyubiquitylated proteins, thus linking substrates to the appropriate degradation machinery¹⁶.

56 Numerous types of selective autophagy have been examined, and much progress has been
57 made in determining the basis of cargo selectivity. The autophagy receptor proteins, OPTN,
58 NDP52, TAX1BP1 and p62 are known to be important in xenophagy^{24,25}, while OPTN, NDP52,
59 and to a lesser extent, TAX1BP1 are essential for PINK1/Parkin-mediated mitophagy^{17,26,27}. A
60 screen in yeast identified the ATG8 and UB-binding protein, CUET, and its mammalian
61 homologue, TOLLIP, to contribute to autophagic removal of expanded polyQ isoforms of
62 huntingtin²⁸. NBR1 and p62 are linked to aggrephagy in mammalian cells²⁹; however, p62 and
63 NBR1 knockout (KO) mice exhibit only a mild increase in ubiquitylated aggregates suggesting
64 that additional receptors are involved³⁰. To identify such autophagy receptor proteins, we
65 examined production and clearance of puromycin-induced truncated and misfolded proteins in
66 the cytosol³¹, termed “DRiPs” for defective ribosomal products³² in individual and
67 combinatorial knockouts of the autophagy receptor proteins, NBR1, p62, NDP52, OPTN, and
68 TAX1BP1 (Fig. 1A, 1B, 1C, Supplementary Fig. 1A). Consistent with the literature^{33,34}, we
69 found a drastic reduction in puromycin-induced foci formation in p62 KO and NBR1 KO cell
70 lines, as well as in NDP52 KO cells compared to WT cells after 2h puromycin (Fig. 1C, 1D, 1E).
71 Though aggregate formation was decreased in NBR1 and NDP52 KO cell lines, any foci that did
72 form were effectively cleared after 3h washout of puromycin (Fig. 1C, 1F, 1G). In contrast,
73 individual OPTN KO and TAX1BP1 KO cell lines showed robust UB-positive foci formation,
74 equal to or greater than WT cells after 2h puromycin (1C, 1D, 1E) and a significant block in
75 aggregate clearance after puromycin washout. More than twice as many cells with foci (~54%)
76 persisted in OPTN KO cells compared to WT (~22%), while in TAX1BP1 KO cells, nearly 4
77 times as many cells retained foci (~85%) (Fig. 1C, 1F, 1G). In TAX1BP1 KO cells with foci, the
78 number of foci per cell, although equivalent to WT at 2h puromycin (Supplementary Fig. 1B,
79 1C), was substantially higher than WT cells upon puromycin washout, indicating a block in

80 clearance (Supplementary Fig. 1D). Distinct roles therefore exist for autophagy receptors in
81 protein aggregate formation and clearance and our data reveal a new autophagy receptor
82 involved in aggregate clearance.

83 We observed complementary results upon exposure of cells to low levels of proteasome
84 inhibition which induces accumulation of misfolded protein into juxtannuclear aggresome-like
85 structures removed via autophagy¹. Imaging revealed decreased UB-labeled foci formation in
86 p62 KO, NBR1 KO and NDP52 KO cells (Supplementary Fig. 1E). Similarly, immunoblot of
87 cellular lysates after fractionation revealed no accumulation of insoluble UB-positive protein in
88 the p62 KO and decreased levels in NBR1 KO and NDP52 KO cells relative to WT cells (Fig.
89 1H, Supplementary Fig. 1F, 1G). However, in OPTN KO and TAX1BP1 KO cells, imaging
90 revealed greater UB-foci accumulation than in WT cells (Supplementary Fig. 1E). Consistent
91 with these observations, UB-conjugated protein was increased in the insoluble fraction of
92 TAX1BP1 KO (~4X increase) and OPTN KO (~2X increase) compared to WT cells (Fig. 1H,
93 Supplementary Fig. 1F), consistent with a block in aggrephagy.

94 We compared accumulation of UB-positive punctae upon short term exposure to MG132
95 or Bafilomycin A, an autophagy inhibitor, to determine whether there is basal accumulation of
96 misfolded or aggregated protein in TAX1BP1 KO cells. We saw little effect in WT cells (Fig. 1I,
97 1J); but in TAX1BP1 KO cells, both inhibitors resulted in formation of UB-positive foci (Fig. 1I,
98 1J), though MG132 to a much greater extent (Fig. 1I, 1J). This implies that the UPS is
99 compensating for an increased basal proteotoxic load in TAX1BP1 KO cells, most likely due to a
100 block in TAX1BP1-mediated selective aggrephagy. Interestingly, proteotoxic stress induced a
101 dramatic increase in TAX1BP1 protein levels (Fig. 2A, 2B). Additionally, a large proportion of
102 TAX1BP1 accumulates with insoluble ubiquitinated protein after MG132 treatment (Fig. 2C).

103 TAX1BP1, NDP52, and CALCOCO1 are paralogous proteins of the CALCOCO gene
104 family, all containing a SKICH domain, a putative canonical LC3-interacting region (LIR) motif
105 and coiled-coil regions while differing in conservation of the C-terminal zinc finger domains in
106 various species²⁵. Therefore, we suggest that the specificity of TAX1BP1 and NDP52 may have
107 diverged over time, leading to a specific function for TAX1BP1 in aggrephagy. TAX1BP1 is the
108 most evolutionarily conserved member of the CALCOCO gene family and present widely in
109 vertebrates, unlike NDP52 which is sporadically lost or truncated²⁵. Examination of NDP52 and
110 TAX1BP1 expression levels in a panel of human tissue lysates revealed that TAX1BP1 is highly
111 expressed in brain, while NDP52 was undetectable and likely does not function in neuronal
112 tissues (Fig. 2D). We then examined primary rat cortical neurons exposed to proteotoxic stress.
113 As in HeLa cells, UB-conjugated protein accumulated in the insoluble fraction upon MG132
114 exposure (Fig. 2E). As in human tissue, TAX1BP1 was expressed robustly in the rat cortical
115 neuron lysate and furthermore, accumulated to a greater extent in the insoluble fraction with
116 increased exposure to proteotoxic stress compared to other autophagy receptor proteins except
117 p62 (Fig. 2F). Consistent with our observations in HeLa cells, TAX1BP1 staining was diffuse in
118 untreated primary rat cortical neurons and in neurons derived from human induced pluripotent
119 stem cells (iPSCs)³⁵, but colocalized robustly with UB upon MG132 treatment (Supplemental
120 Fig. 2A, 2B). To our knowledge, this is the first study to identify a role for TAX1BP1 in
121 aggrephagy and suggests that TAX1BP1 plays a specific role in neuronal aggrephagy.

122 To further validate a specific role for TAX1BP1 in aggrephagy, we reintroduced GFP-
123 TAX1BP1 at near endogenous levels in the TAX1BP1 KO HeLa cell line (Supplementary Fig.
124 3A). In untreated cells, GFP-TAX1BP1 was diffuse or present in small punctae (Fig. 3A) and
125 colocalized with UB-positive foci upon 2h puromycin treatment (Fig. 3A). After puromycin

126 washout, UB foci were cleared to a similar extent in the TAX1BP1-rescued TAX1BP1 KO cells
127 as in WT cells and GFP-TAX1BP1 returned to a diffuse or punctate appearance (Fig. 3A, 3B).

128 To further confirm the effect of TAX1BP1 on aggregate clearance, we titrated expression
129 of N- or C-terminally tagged TAX1BP1 constructs in the TAX1BP1 KO background to create
130 stable high- or low-expressing rescue lines (Supplementary Fig. 3A, 3B). Aggregate formation
131 and clearance was similar to WT in the low-expressing TAX1BP1 rescue lines (Fig. 3C, 3D,
132 Supplementary Fig. 3B). However, upon 2h puromycin treatment, UB-positive foci were present
133 in only ~20% of the high TAX1BP1-expressing rescue cell lines compared to ~65% of WT and
134 ~90% of TAX1BP1 KO cells. (Fig. 3C). Furthermore, upon puromycin washout, foci were
135 cleared to a greater extent in TAX1BP1 high-expressing rescue lines in which only ~5-10% of
136 cells retained aggregates compared to 30% in WT cells, and >70% in the parental TAX1BP1 KO
137 (Fig. 3D), suggesting an active role for TAX1BP1 in promoting aggregate clearance.

138 Because we did not observe robust foci formation in the high-expression TAX1BP1-
139 rescue lines (Fig. 3C, Supplementary Fig. 3B), we treated cells with Bafilomycin A during
140 puromycin treatment and washout to block autophagy. In WT cells, Bafilomycin A resulted in
141 increased aggregate retention after washout (Fig. 3E, 3F, larger field of view shown in
142 Supplementary Fig 3C). However, in TAX1BP1 KO cells, Bafilomycin A barely exacerbated the
143 defect in aggregate clearance, suggesting that the autophagy pathway is nonfunctional in the
144 presence of proteotoxic stress (Fig. 3E, 3F). Bafilomycin A was sufficient to restore UB-positive
145 foci in TAX1BP1 rescue cell lines (Fig. 3E, 3F, Supplementary Fig. 3C), resulting in UB-
146 positive foci which colocalized with FLAG-TAX1BP1 and tended to loosely accumulate in the
147 perinuclear region, similar to that observed upon addition of Bafilomycin A to WT cells (Fig. 3E,
148 Supplementary Fig. 3D). Our data demonstrate that TAX1BP1-mediated aggregate clearance is

149 dependent upon expression level and capable of accelerating degradation of insoluble protein
150 aggregates by promoting selective flux through the autophagy pathway.

151 TAX1BP1 contains several protein-interacting domains, including an N-terminal SKICH
152 domain, at least 3 less studied coiled-coil regions, a canonical LIR motif and putative
153 noncanonical CLIR motif, as well as two C-terminal zinc finger (ZF) UB-binding
154 domains^{24,25,27,28}. We created a variety of truncation and point mutants to test the requirements
155 for these domains in TAX1BP1-mediated aggrephagy (Fig. 4A). Each mutant was stably
156 expressed in the TAX1BP1 KO background and assessed for puromycin-induced aggregate
157 formation and clearance. Aggregate formation occurred with minor variation similarly in WT
158 and all mutant cell lines as well as a GFP-only control (Fig. 4Bi,ii, 4C, larger fields in
159 Supplementary Fig. 4A). However, substantial differences were observed amongst the mutants in
160 aggregate clearance. N-terminal SKICH deletion (Δ SKICH) as well as both the LIR (W49A) and
161 CLIR (V143S) point mutants localized to UB-positive foci and rescued clearance to the same
162 extent as WT TAX1BP1 (Fig. 4Biii, iv, v, 4D, Supplementary Fig. 4A). The structure of the
163 TAX1BP1 SKICH domain shows that the canonical LIR (W49) is mostly buried within the
164 hydrophobic interior of the folded SKICH domain and therefore is likely not a functional LIR
165 domain³⁶. A truncation mutant lacking both C-terminal ZF domains did not localize to
166 puromycin-induced foci and was unable to rescue aggregate clearance (Fig. 4Bvi, 4D). To
167 determine whether one or both ZF domains was essential, we created point mutants targeting
168 both ZF domains (ZF1/ZF2: Q743A/E747K/ Q770A/E774K) as well as each domain
169 individually (ZF1:Q743A/E747K, ZF2:Q770A/E774K). The double mutant, ZF1/ZF2, as well as
170 the single ZF2 mutant, failed to localize to UB foci after puromycin treatment and both were
171 unable to rescue aggregate clearance (Fig. 4Bviii, ix, 4D). In contrast, point mutation of ZF1 had
172 little effect on TAX1BP1 localization and rescued aggregate clearance similarly to WT

173 TAX1BP1 (Fig. 4Bvii, 4D). This is consistent with a prior report that only the ZF2 of TAX1BP1
174 is capable of binding UB²⁵. An N- and C-terminally truncated mutant (Δ SKICH/ Δ ZF) did not
175 localize to aggregates but instead formed aberrant clusters in the cytosol and was inferior to the
176 ZF mutants in its ability to rescue clearance (Fig. 4Bx, 4D, Supplementary Fig. 4A).

177 Very similar results were observed in triple knockout (TKO: TAX1BP1 KO, OPTN KO,
178 NDP52 KO) cells (Supplementary Fig. 4B, 4C), ruling out potential redundancy that may mask
179 requirements for TAX1BP1 domains through functionally related autophagy receptors. Low,
180 near-endogenous expression of TAX1BP1 rescued aggregate clearance to that of WT cells while
181 higher expression increased clearance compared to WT cells (Fig. 4E, 4F, Supplementary Fig.
182 4C). In contrast, neither the Δ SKICH, Δ ZF nor Δ SKICH/ Δ ZF mutants were able to fully rescue
183 aggregate clearance demonstrating the need for these protein-interaction and UB-binding
184 domains (Fig. 4F, Supplementary Fig. 4C). Thus, full length TAX1BP1 was able to rescue
185 aggregate clearance in the absence of NDP52 and OPTN, indicating that TAX1BP1 promotes
186 aggregate clearance (Fig. 4F).

187 We also examined whether TAX1BP1 overexpression in WT cells beyond the level of
188 endogenous TAX1BP1 expression could promote aggregate clearance, thus addressing the
189 therapeutic potential of TAX1BP1. TAX1BP1 protein expressed in WT cells behaved similarly
190 to the endogenous protein, remaining diffuse in untreated cells and colocalizing with UB-stained
191 foci upon puromycin treatment (Fig. 4G, Supplementary Fig. 4D). Aggregate formation upon 2h
192 puromycin treatment was decreased in both low (~20% decrease) and high (~30% decrease) -
193 overexpressing TAX1BP1 cells (Fig. 4H). Clearance of aggregates in WT cells with low
194 overexpression of TAX1BP1 was similar to that in WT cells expressing only endogenous
195 TAX1BP1 (Fig. 4I, Supplementary Fig. 4D), whereas, higher levels of TAX1BP1 expression

196 increased clearance upon puromycin washout – only ~10% of cells retained UB-positive foci in
197 contrast to more than 30% of WT cells (Fig. 4G, 4I).

198 Overexpression of WT TDP-43 and polyQ huntingtin fragments is cytotoxic in *in*
199 *vitro* and *in vivo* model system^{20,37–44}. Stimulation of autophagy increases clearance of WT
200 and mutant TDP-43, huntingtin fragments and attenuates cytotoxicity^{20,43,45–48}. Therefore, WT,
201 TAX1BP1 KO, and high-expressing TAX1BP1-rescue cells were exposed to a variety of
202 stresses, including low dose proteasome inhibition and expression of aggregation-prone proteins,
203 such as the ALS-associated, EGFP-TDP-43, and varied length model substrates carrying
204 expanded glutamine tracts (polyQ) expressed from exon 1 of the huntingtin-encoding gene
205 (Supplementary Fig. 5A, 5B). Cells were either infected or transfected on day 1 and assessed
206 daily for six days. Loss of TAX1BP1 decreased viability compared to WT cells upon exposure to
207 each form of proteotoxic stress (Fig. 5A, Supplementary Fig. 5C). Expression of TAX1BP1 in
208 the knockout line was able to partially restore cell viability (Fig. 5A, Supplementary Fig. 5C).

209 To determine whether TAX1BP1 can aid in clearance of Htt-polyQ proteins, we infected
210 WT, TAX1BP1 KO, and TAX1BP1-rescue cells with virus to express HttQ23-EGFP, HttQ74-
211 EGFP and HttQ103-EGFP and assessed aggregate levels 4 days post-infection (Supplementary
212 Fig. 5A). Due to the low number of glutamine repeats, HttQ23-EGFP does not form inclusions
213 and therefore is a useful control when comparing to the aggregate-forming HttQ74-EGFP and
214 HttQ103-EGFP proteins. HttQ23-EGFP expression was robust and as expected the protein
215 remained largely diffuse and cytosolic in both WT and TAX1BP1 KO cells (Fig. 5B). In
216 contrast, TAX1BP1-deficient cells exhibited increased focal aggregates of both Htt74Q-EGFP
217 and Htt103Q-EGFP compared to WT cells (Fig. 5B, 5C, 5D). Rescue of the TAX1BP1 KO line
218 with expression of FLAG-TAX1BP1 restored clearance of HttQ74-EGFP and Htt103Q-EGFP to
219 that of WT cells, indicating that TAX1BP1 is highly effective in directing clearance of

220 huntingtin polyQ proteins (Fig. 5B, 5C, 5D). Endogenous TAX1BP1 also colocalized with
221 HttQ103-EGFP aggregates in WT cells (Fig. 5E) appearing to enclose aggregates in many
222 instances (Fig. 5F, Supplementary Figure 5D).

223 Because TAX1BP1 overexpression can promote clearance of aggregates beyond that in
224 WT cells and because we found TAX1BP1 highly and specifically-expressed in brain (Figure
225 2D, 2F), we examined whether TAX1BP1 could provide a protective effect in iPSC-derived
226 neurons exposed to huntingtin proteins. iPSC-derived neurons with or without stable expression
227 of TAX1BP1 were infected with virus expressing either the non-aggregating control construct,
228 HttQ23-EGFP, (Figure 5G) or the aggregate-forming HttQ103-EGFP (Figure 5H) and imaged
229 daily for 15 days to assess viability via nuclei count (NLS-BFP). The rates of cell death, assessed
230 by comparing slopes obtained from lines fitted to cell number over time, did not differ between
231 WT and TAX1BP1-overexpressing neurons infected with the non-aggregate-forming HttQ23-
232 EGFP (Figure 5G). However, TAX1BP1 overexpression significantly improved survival in
233 neurons exposed to the aggregate-forming HttQ103-GFP protein (Figure 5H), consistent with our
234 observations in HeLa cells.

235 Here we report a broad role for TAX1BP1 in protein homeostasis. Our results
236 demonstrate that loss of TAX1BP1 leads to decreased ability to target insoluble protein for
237 degradation. Overexpression of TAX1BP1 further promotes aggregate clearance and rescues cell
238 viability upon exposure to varied proteotoxic insults, including translation stress, proteasome
239 inhibition, and exposure to aggregate-prone proteins such as TDP-43 and huntingtin-expanded
240 polyQ model substrates (Supplementary Figure 5E).

241 Aggrephagy has potential to mitigate neurodegenerative proteinopathies. Focus on the
242 proteins that provide specificity in targeting aggregates, such as TAX1BP1, may be valuable, as
243 these are likely deciding factors in directing the autophagy response. Using single or

244 combinatorial knockouts of OPTN, NDP52, TAX1BP1, NBR1, and p62, we observed distinct
245 roles for these varied autophagy receptor proteins in aggrephagy. Though they may function *en*
246 *masse* to maintain protein homeostasis, the individual proteins exhibit functional and spatial
247 distinctions at the subcellular and tissue level. For example, autophagy receptor proteins are
248 recruited independently to distinct microdomains surrounding bacteria and mitochondria where
249 they perform nonredundant roles during xenophagy and mitophagy, respectively^{26,49}.
250 Furthermore, TAX1BP1 is robustly expressed in human brain lysate as well as primary rat
251 cortical neurons, distinguishing it from NDP52. TAX1BP1 is also associated with the insoluble
252 protein fraction in primary rat cortical neurons exposed to proteotoxic stress. Amongst the other
253 autophagy receptor proteins, only p62 showed similar association with the insoluble fraction.
254 TAX1BP1 and its paralog, NDP52, share similar domain structures; however, recent studies
255 suggest structural differences in the organization of the SKICH domains as well as distinct
256 ATG8 binding affinities^{25,50}. TAX1BP1 is also more broadly conserved than NDP52 among
257 mammals²⁵, suggesting that TAX1BP1 fills nonredundant essential roles. Future studies
258 examining TAX1BP1 expression levels during aging and in animal models of neurodegenerative
259 disease are warranted.

260 TAX1BP1 recruitment to protein aggregates requires the C-terminal ubiquitin-binding
261 domain and its function in promoting aggrephagy further necessitates the N-terminal SKICH
262 domain. However, none of our TAX1BP1 mutants were completely dead in terms of rescue
263 effect, suggesting that other cellular functions of TAX1BP1 may be involved. One such role is to
264 act as a Myosin VI cargo adaptor protein for mediating autophagosome maturation, which could
265 contribute to clearance dependent upon other upstream factors, thus explaining partial rescue²⁵.
266 Additionally, TAX1BP1 is best studied for its role in negatively regulating nuclear factor- κ B
267 (NF- κ B) and interferon regulatory factor (IRF) 3 via an interaction with the deubiquitinase, A20,

268 thus restricting pro-inflammatory signaling and immune response^{51,52}. Though links between
269 TAX1BP1's role as an autophagy adaptor and the immune response are yet to be understood, it
270 is well known that protein aggregation, inflammation, and autophagy are intertwined⁵³. Studies
271 have shown that exposure to disease-associated protein aggregates can elicit innate immune
272 response in glial cells and that LPS-induced inflammation results in enhanced aggregate
273 formation in disease models suggesting a synergistic relationship between proinflammatory
274 response, proteostasis and neurodegeneration^{54,55}. Autophagy may function to downregulate
275 inflammatory signaling and TAX1BP1 may be an important link between detection and
276 monitoring of cellular protein aggregates and the inflammatory response.

277 Notably, ectopic expression of TAX1BP1 in knockout cells was able to rescue aggregate
278 clearance to WT levels and increased overexpression of TAX1BP1 in both the knockout and WT
279 cells was able to reduce aggregate levels below those observed in WT cells. Furthermore,
280 TAX1BP1 overexpression in iPSC-derived neurons was protective against huntingtin aggregate-
281 induced toxicity. TAX1BP1 thus plays a general role in promoting autophagy and future studies
282 aimed at increasing TAX1BP1 expression or stability *in vivo* present promising therapeutic
283 potential in addressing proteinopathies. An increased understanding of targeting specificity of
284 selective autophagy receptor proteins for protein aggregates may make autophagy-stimulating
285 approaches more specific and effective in treatment of protein misfolding diseases.

286

287 **Acknowledgements**

288 We thank Drs. Alicia Pickrell, Malavika Raman, Achim Werner, David Beck and Richa Lomash
289 for critical reading of the manuscript. We also thank the NINDS Light Imaging Facility, the
290 NICHD Imaging Facility, and the NHLBI Flow Cytometry Core Facility. We thank Dr. Harm
291 Kampinga for sharing the EGFP-HttQ43 and EGFP-HTTQ74 plasmids, John Badger and Dr.

292 Katherine Roche for providing the primary rat cortical neurons and expertise. This work was
293 supported in part by the National Institutes of Health Grants NINDS intramural program (R.J.Y)
294 and NIGMS Postdoctoral Research Associate Fellowship (S.A.S.).

295

296 **Author Contributions**

297 S.A.S. and R.J.Y. conceived the project; S.A.S. and R.J.Y. designed experiments; S.A.S and
298 H.V.S. performed experiments; G.K. performed image analysis for neuron viability; M.E.W.
299 provided iPSCs and relevant expertise, S.A.S and R.J.Y. wrote the manuscript and all authors
300 contributed to editing the manuscript.

301

302 **Competing Interests**

303 The authors declare no competing financial interests.

304 **Methods**

305 **Cell Culture and reagents**

306 HeLa and HEK293T were cultured in DMEM (Life Technologies) supplemented with
307 10% (v/v) FBS (Gemini Bio Products), 10 mM HEPES (Life Technologies), 1 mM sodium
308 pyruvate (Life Technologies), 1mM non-essential amino acids (Life Technologies) and 2 mM
309 glutamine (Life Technologies). HeLa cells were acquired from the ATCC and authenticated at
310 the Johns Hopkins GRCF Fragment Analysis Facility using STR profiling. Testing for
311 mycoplasma contamination was performed bimonthly using the Plasmotest kit (InvivoGen).
312 Plasmids were transfected using either X-tremeGENE 9 (Roche), polyethylenimine
313 (Polysciences) or Avalanche-OMNI (EZ Bio-systems). Primary cultured cortical neurons were
314 isolated from male and female embryonic day 18 Sprague-Dawley rats and maintained in
315 Neurobasal medium (Gibco) supplemented with 2mM glutamine (Life Technologies) and B-27
316 Supplement (Gibco). All rat procedures were performed according to a protocol (#1171)
317 approved by the National Institutes of Health NINDS Institutional Animal Care and Use
318 Committee. Primary neurons were treated with MG132 on day-in-vitro (div) 10.

319 For puromycin (Invivogen), MG132 (Sigma-Aldrich) or Bafilomycin A (Sigma-Aldrich)
320 treatments, cells were treated with the indicated concentrations of drug in full media and either
321 harvested as described or washed three times in full media and returned to full media for the
322 indicated durations.

323

324 **Antibodies**

325 Rabbit mono- and polyclonal antibodies used for immunoblotting include: NDP52 (CST,
326 60732S), TAX1BP1 (CST, 5105S), Actin (CST, 4967S); GAPDH (Sigma, G9545-200UL),
327 OPTN (Proteintech, 10837-I-AP) and TAX1BP1 (Sigma, HPA024432); rabbit antibodies used

328 for immunofluorescence include TAX1BP1 (Sigma, HPA024432). Mouse Monoclonal
329 antibodies used for immunoblotting were: GFP (Roche, 11814460001), ubiquitin (Millipore,
330 MAB1510), NBR1 (Abnova, H00004077-M01) and p62 (Abnova, H00008878-M01); mouse
331 antibodies used for immunofluorescence include ubiquitin FK2 (Biomol International, PW8810-
332 0500). Secondary AlexaFluor® (ThermoFisher) conjugated antibodies were incubated for 1h RT
333 at 1:1000. DAPI counterstain (ThermoFisher) at 300nM was incubated for 10 min RT.

334

335 **TALEN and CRISPR gene knockout cell lines**

336 Construction of OPTN, NDP52, TAX1BP1, TKO and pentaKO knockout HeLa lines
337 were reported previously ¹⁷. All knockout lines were generated using CRISPR guide RNAs
338 (gRNAs) chosen to target one or more exons common to all splicing variants of the gene of
339 interest (all information listed in Supplementary Table S1). Oligonucleotides (Operon)
340 containing CRISPR target sequences were annealed and ligated into the linearized
341 gRNA_Cloning vector which was a gift from George Church (Addgene #41824) or SpCas9-2A-
342 Puro, which was a gift from Feng Zhang (Addgene #48139). HeLa cells were cotransfected using
343 XtremeGENE9 (Roche) with either the the gRNA_Cloning vector, pCDNA YFP-C1, and the
344 hCas9 plasmid, which was a gift from George Church (Addgene #41815) or with SpCas9-2A-
345 Puro. Forty-eight hours post-transfection, YFP-positive cells were isolated either via
346 fluorescence activated cell sorting or puromycin selection and serially diluted for single colony
347 clones. Single colonies were expanded and screened for depletion of the targeted gene product
348 by immunoblotting. DNA was extracted using the Zymo gDNA Isolation Kit and genotyped
349 using primers targeting fragments of the genomic DNA from knockout clones containing the
350 putative cleavage site (primers and sequences in Supplementary Table 1).

351

352 **Cloning and generation of stably infected cell lines**

353 The Gateway Cloning (Life Technologies) system was used to generate pHAGE-GFP-
354 TAX1BP1, pHAGE-N-FLAG-HA-TAX1BP1, and pHAGE-GFP-TDP43. Briefly, genes of
355 interest were cloned into pDONR223 then recombined into destination vectors pHAGE-N-
356 FLAG-HA or pHAGE-N-GFP using L Recombinase (Life Technologies) as per the
357 manufacturer's protocol. Mutations in cDNA sequences were introduced using PCR site-directed
358 mutagenesis in the pDONR223 vector. All constructs generated in this study were verified by
359 sequencing. Original plasmids containing EGFP-HttQ43 and EGFP-HttQ74 were kindly
360 provided by Dr. Harm Kampinga (Groningen, Netherlands). pYES2/103Q was a gift from
361 Michael Sherman (Addgene plasmid #1385) and pEGFP-Q23 was a gift from David Rubinzstein
362 (Addgene plasmid #40261). All huntingtin protein constructs were cloned into pLEX-EF1 α -
363 EGFP for lentiviral expression. pDONR-TDP-43 WT YFP was a gift from Aaron Gitler
364 (Addgene plasmid #27470). Primer sequences are available upon request.

365 For generation of stable cell lines, lentiviruses (pHAGE- vectors) were packaged in
366 HEK293T cells. HeLa cells were transduced with virus for 24 hours with 8 μ g/ml polybrene then
367 selected for protein expression by drug-resistance (puromycin or blasticidin) or fluorescence
368 activated cell sorting. Generation of low- and high-expressing cells was done via infection with
369 various dilutions of virus and expression assessed via comparison to endogenous protein levels
370 on immunoblot.

371

372 **Aggregate formation and clearance studies**

373 For acute treatments, HeLa cells were grown on poly-D-lysine-coated (Sigma-Aldrich,
374 P7280) coverslips and treated with either 5 μ g/ml of puromycin (Invivogen) for 2 h or 1 μ M
375 MG132 (Sigma-Aldrich) for 8 h at 37°C. Cells were either fixed for imaging or assessed for

376 clearance. For clearance, cells were washed three times in DMEM–10% FBS and released into
377 drug-free medium for 3 h at 37°C. For long treatments, HeLa cells were grown on poly-D-lysine-
378 coated coverslips and treated with 1 µg/ml of puromycin or 1 µM MG132 for 18 h at 37°C.
379 Coverslips were fixed and processed for microscopy, as outlined above.

380 For huntingtin poly-Q-protein clearance assays, HeLa cells were seeded on poly-D-
381 lysine-coated coverslips and transduced the following day with lentivirus expressing either
382 HttQ23-EGFP, HttQ74-EGFP or HttQ103-EGFP for 24 hours with 8 µg/ml polybrene. Cells
383 were fixed for imaging and assessed 4 days post-infection.

384

385 **Subcellular fractionation**

386 Cells were washed once and scraped in cold PBS, pelleted, and lysed in RIPA buffer
387 (ThermoFisher, 89900) supplemented with Complete Protease Inhibitor Cocktail (Roche), 1mM
388 EGTA, 1mM EDTA, 100mM chloroacetamide (Sigma-Aldrich) and 100mM DTT for 15
389 minutes at 4°C with end over end rotation. Five to ten percent of the total volume was collected,
390 mixed with 4X LDS (Life Technologies), boiled, and reserved for the input fraction. RIPA-
391 soluble fraction was obtained after centrifugation at 20,000 rpm for 15 min at 4°C, 4X LDS was
392 added, and samples were heated to 99°C with shaking for 10 minutes. The insoluble fraction
393 consisting of the remaining pellet was washed once with lysis buffer, spun at 20,000 rpm for 10
394 min at 4°C, then lysed in 1X LDS, 100mM DTT in PBS and heated to 99°C with shaking for 15
395 minutes. Protein concentration was determined via DC Protein Assay (BioRad). Soluble and
396 insoluble fractions were normalized to the protein concentration of the input fraction. For
397 analysis, 10-15% of RIPA-soluble fraction and 2.5-5% of insoluble fraction were loaded on 4-
398 12% Bis-Tris gels and run using MOPS buffer (Life Technologies) and visualized by western
399 blotting on PVDF. Western blotting was performed by wet transfer method in either NuPage

400 transfer buffer or Tris-glycine transfer buffer (Life Technologies). Proteins were detected using
401 horseradish peroxidase-coupled secondary antibodies (GE Healthcare Life Sciences, Piscataway,
402 NJ) and ECL Plus or ECL Prime western blotting detection reagents (GE Healthcare Life
403 Sciences). Images were acquired using an MP gel documentation system (Bio-Rad Laboratories).
404 Quantification of immunoprecipitation bands was performed using the volume tools in Image
405 Lab software (Bio-Rad Laboratories).

406

407 **Immunoblotting**

408 After the indicated treatments, cells were harvested by scraping in cold PBS and either
409 fractionated as described above or lysed in 2% SDS/1X PBS, heated to 99°C with shaking for 10
410 minutes, and spun at 20,000 rpm for 15 min at RT. Protein concentration was determined using
411 DC Protein Assay (BioRad) and 20-50 ug of protein per sample was separated on 4–12% Bis-
412 Tris gels using MOPS or MES running buffer (Life Technologies). Western blotting was
413 performed by wet transfer method in either NuPage transfer buffer or Tris-glycine transfer buffer
414 (Life Technologies). Proteins were detected using horseradish peroxidase-coupled secondary
415 antibodies (GE Healthcare Life Sciences, Piscataway, NJ) and ECL Plus or ECL Prime western
416 blotting detection reagents (GE Healthcare Life Sciences). Images were acquired using an MP
417 gel documentation system (Bio-Rad Laboratories). Quantification of immunoprecipitation bands
418 was performed using the volume tools in Image Lab software (Bio-Rad Laboratories). Human
419 tissue panel blot was purchased (NOVUS Biologicals).

420

421 **Immunofluorescence Microscopy**

422 HeLa cells were seeded on poly-D-lysine-coated (Sigma-Aldrich, P7280) coverslips and
423 treated as indicated. Following treatment, cells were fixed at room temperature in 4%

424 paraformaldehyde for 15 minutes, permeabilized and blocked with filtered IF buffer (0.1%
425 Triton X-100, 3% goat serum, 1X PBS) for 1 hour at RT. For immunostaining, cells were
426 incubated with indicated antibodies diluted in IF buffer overnight at 4°C, washed 3 times with IF
427 buffer and incubated with Alexa Fluor-conjugated secondary antibodies (Life Technologies)
428 1:1000 in IF buffer for 1 hour at RT. Cells were then incubated with DAPI (Sigma) diluted in IF
429 buffer at 1:10,000 for 10 minutes at RT. Cells were washed 2 times with IF buffer and 1 time
430 with 1X PBS. Coverslips were mounted on slides using Prolong Gold Antifade (Life
431 Technologies). Representative images were collected with an inverted laser scanning LSM 880
432 microscope (Carl Zeiss) using a 63X/1.4 objective Plan-Apochromat (Carl Zeiss). Images were
433 collected as z-stacks captured at optimal thickness. Representative images shown are maximum
434 intensity projections unless otherwise noted.

435

436 **Cell viability and Growth curve**

437 For HeLa cell viability assays, cells were seeded in quadruplicate in white clear-bottom
438 96-well plates (Corning). The next day, cells were treated as indicated in figure legends. Cell
439 viability was measured by using the Cell Titer-Glo system (Promega) according to the
440 manufacturer's instructions. Values were normalized to the value for untreated samples for each
441 cell line. Means and standard deviations were calculated, and statistical significance was
442 calculated using one-way analysis of variance (ANOVA). One plate was measured each day
443 using a Synergy H1Hybrid Multi-Mode Reader (Biottek).

444

445 **Statistical analysis for aggregate formation and clearance assays**

446 For quantification, cells with puromycin-, MG132-, or HTT-induced foci were either
447 counted manually in a blinded fashion or using the particle analysis plug-in in ImageJ. Macros

448 created are available on request. At least 200 cells per sample were analyzed in three biological
449 replicate studies. The number of observations used in each experimental series is included in
450 Table 1. Means and standard deviations were calculated, and statistical significance was
451 assessed. For comparisons between three or more groups, a one or two way-ANOVA with
452 Tukey's post-hoc analysis was performed using Prism V7 (GraphPad Software) as noted in the
453 figure legend. Error bars represent standard deviation (SD): * $P < 0.05$, ** $P < 0.01$, *** $P < 0.001$,
454 **** $P < 0.0001$. The number of observations used in each experimental series was included in the
455 figure legend or can be found in Table 1. All test statistics (e.g. F), degrees of freedom and P
456 values are included in Table 1. Three biological replicates were performed for each experiment.
457 To determine number of foci per individual cell, CellProfiler⁵⁶, version 2.2.0 was used. All
458 CellProfiler pipelines and detailed settings to reproduce the image analysis procedures are
459 available upon request.

460

461 **Neuron Culture and Viability Assay**

462 Induced pluripotent stem cells (iPSCs), parental line WTC11, were maintained in
463 Essential 8 Flex medium (Gibco, A28583-01) supplemented with Essential 8 Flex Supplement
464 (Gibco, A28584-01). iPSCs were grown on Matrigel-coated plates (Corning, 354277) and cell
465 dissociation was performed using Accutase (StemCell Technologies, 07920). Stable expression
466 of NLS-BFP (used for nuclei counting) was obtained by infecting cells with lentivirus expressing
467 U6-NLS-BFP followed by sorting for BFP-positive cells. Stable expression of TAX1BP1 was
468 obtained by infecting NLS-BFP-expressing cells with lentivirus expressing EF1 α -FLAG-
469 TAX1BP1 followed by puromycin selection.

470 For the viability assay, iPSCs grown in 6-well plates were infected with lentivirus
471 expressing EF1 α -HttQ23-EGFP or EF1 α -HttQ103-EGFP, the following day, media was

472 changed, and cells were allowed to recover for 1 day. Two days post-infection, cells were plated
473 in induction medium: DMEM/F12 with HEPES (Gibco, 11330032) containing N2 Supplement
474 (100X) (Gibco, 17502048), non-essential amino acids (100x) (Gibco, 11140050), glutamax
475 (100X) (Gibco, 35050061), ROCK inhibitor Y-27632 (10mM) (Tocris, 1254), and
476 doxycycline (2mg/ml) (Sigma, D9891). Induction medium was changed daily for 2 days. On
477 day 3 post-induction, cells were dissociated using Accutase, counted, and plated at 50,000
478 cells/well in poly-L-ornithine-coated (PLO) (Sigma, P3655) 96-well plates (Perkin Elmer,
479 6055302) in BrainPhys neuronal medium (StemCell Technologies, 05790) containing B27
480 supplement (50X) (Gibco, 17504044), BDNF (10µg/ml) (PeproTech, 450-02), NT-3 (10µg/ml)
481 (PeproTech, 450-03), and laminin (1µg/ml) (Gibco, 23017015). Half of the well volume was
482 removed and replaced with fresh supplemented BrainPhys media every 3 days for the duration of
483 the assay. iPSCs-derived neurons were imaged daily for 20 days. Sixteen fields of view were
484 imaged per each well of three independent biological replicates. Cells were imaged using a 20X
485 air objective (NA 0.75) with 1.5X optical zoom on a Nikon Ti-2 CSU-W1 spinning disk system
486 with a photometrics 95B camera operated by Nikon Elements software equipped with
487 temperature regulation and CO₂ control.

488

489 **Statistical Analysis for Neuron Viability Assay**

490 To determine iPSC-derived neuron survival, NLS-BFP-expressing nuclei were counted
491 automatically using the R EBImage package⁵⁷. Three biological replicates per condition were
492 pooled together and the data were fitted to an exponential decay model using the R DRC
493 package⁵⁸ and the formula: $f(x) = c + (d-c)(\exp(-x/e))$ where (e) is the slope and (d) and (c)
494 represent the upper and the lower limits around the slope. Outliers were detected and removed
495 using interquartile range using the R Outliers package⁵⁹. The survival score was calculated from

496 the fitted model, in which the slope (ϵ) represents the survival score of each population of cells
497 counted at every time point for the designated treatment. For statistical comparison, a
498 permutation test (a.k.a randomization test) was used. In brief, the delta mean score of the groups
499 was compared to random delta mean scores of shuffled groups iterated 10,000 times. *P* value
500 was determined by calculating the number of times the delta score was higher in the shuffled
501 group than in the ground true group⁵⁸. The number of observations used in each experimental
502 series is included in Table 2. Code is provided in Supplementary Information.

503

504 **Data Availability**

505 The datasets generated for all microscopy cell counting experiments are available as
506 supplementary files and noted in the associated figure legends. The datasets generated and
507 analyzed to assess neuron viability are available from the corresponding author on request.
508 Associated code is available as supplementary files. Figures 1D, 1F, 1J, 3B, 3D, 3F, 4C, 4D, 4E,
509 4F, 4H, 4I, 5A, 5C, 5D, 5G, 5H, and Supplementary Figure 5C have associated raw data
510 included in Tables 1 and 2. There are no restrictions on data availability.

511

512 **Code Availability**

513 Code used to generate datasets and analyze neuron viability is available as supplementary
514 files. All macros created for use with ImageJ/Fiji are available on request. CellProfiler pipelines
515 and detailed settings to reproduce the image analysis procedures are available upon request.

516 **References**

- 517 1. Kopito, R. R. Aggresomes, inclusion bodies and protein aggregation. *Trends in Cell*
518 *Biology* **10**, 524–530 (2000).
- 519 2. Behrends, C. & Fulda, S. Receptor Proteins in Selective Autophagy. *Int. J. Cell Biol.*
520 **2012**, 1–9 (2012).
- 521 3. Ciechanover, A. & Kwon, Y. T. Protein quality control by molecular chaperones in
522 neurodegeneration. *Frontiers in Neuroscience* **11**, (2017).
- 523 4. Rubinsztein, D. C. The roles of intracellular protein-degradation pathways in
524 neurodegeneration. *Nature* **443**, 780–786 (2006).
- 525 5. Mizushima, N. & Komatsu, M. Autophagy: Renovation of cells and tissues. *Cell* **147**,
526 728–741 (2011).
- 527 6. Feng, Y., He, D., Yao, Z. & Klionsky, D. J. The machinery of macroautophagy. *Cell*
528 *Research* **24**, 24–41 (2014).
- 529 7. Hershko, A. & Ciechanover, A. The ubiquitin system. *Annu. Rev. Biochem.* **67**, 425–479
530 (1998).
- 531 8. Wong, E. & Cuervo, A. M. Integration of clearance mechanisms: the proteasome and
532 autophagy. *Cold Spring Harbor perspectives in biology* **2**, (2010).
- 533 9. Sherman, M. Y. & Goldberg, A. L. Cellular defenses against unfolded proteins: A cell
534 biologist thinks about neurodegenerative diseases. *Neuron* **29**, 15–32 (2001).
- 535 10. Lamark, T. & Johansen, T. Aggrephagy: Selective disposal of protein aggregates by
536 macroautophagy. *International Journal of Cell Biology* (2012). doi:10.1155/2012/736905
- 537 11. Salomons, F. A. *et al.* Selective Accumulation of Aggregation-Prone Proteasome
538 Substrates in Response to Proteotoxic Stress. *Mol. Cell. Biol.* **29**, 1774–1785 (2009).
- 539 12. Morimoto, R. I. Proteotoxic stress and inducible chaperone networks in neurodegenerative

- 540 disease and aging. *Genes and Development* **22**, 1427–1438 (2008).
- 541 13. Bennett, E. J., Bence, N. F., Jayakumar, R. & Kopito, R. R. Global Impairment of the
542 Ubiquitin-Proteasome System by Nuclear or Cytoplasmic Protein Aggregates Precedes
543 Inclusion Body Formation. *Mol. Cell* **17**, 351–365 (2005).
- 544 14. Hara, T. *et al.* Suppression of basal autophagy in neural cells causes neurodegenerative
545 disease in mice. *Nature* **441**, 885–9 (2006).
- 546 15. Komatsu, M. *et al.* Loss of autophagy in the central nervous system causes
547 neurodegeneration in mice. *Nature* **441**, 880–884 (2006).
- 548 16. Kirkin, V., McEwan, D. G., Novak, I. & Dikic, I. A Role for Ubiquitin in Selective
549 Autophagy. *Molecular Cell* **34**, 259–269 (2009).
- 550 17. Lazarou, M. *et al.* The ubiquitin kinase PINK1 recruits autophagy receptors to induce
551 mitophagy. *Nature* **524**, 309–14 (2015).
- 552 18. Kraft, C., Deplazes, A., Sohrmann, M. & Peter, M. Mature ribosomes are selectively
553 degraded upon starvation by an autophagy pathway requiring the Ubp3p/Bre5p ubiquitin
554 protease. *Nat. Cell Biol.* **10**, 602–610 (2008).
- 555 19. Khaminets, A. *et al.* Regulation of endoplasmic reticulum turnover by selective
556 autophagy. *Nature* **522**, 354–358 (2015).
- 557 20. Barmada, S. J. *et al.* Autophagy induction enhances TDP43 turnover and survival in
558 neuronal ALS models. *Nat. Chem. Biol.* **10**, 677–685 (2014).
- 559 21. Rubinsztein, D. C., Bento, C. F. & Deretic, V. Therapeutic targeting of autophagy in
560 neurodegenerative and infectious diseases. *J. Exp. Med.* **212**, 979–990 (2015).
- 561 22. Sarkar, S. & Rubinsztein, D. C. Huntington’s disease: Degradation of mutant huntingtin
562 by autophagy. *FEBS J.* **275**, 4263–4270 (2008).
- 563 23. Hjerpe, R. *et al.* UBQLN2 Mediates Autophagy-Independent Protein Aggregate Clearance

- 564 by the Proteasome. *Cell* **166**, 935–949 (2016).
- 565 24. Von Muhlinen, N., Thurston, T., Ryzhakov, G., Bloor, S. & Randow, F. NDP52, a novel
566 autophagy receptor for ubiquitin-decorated cytosolic bacteria. *Autophagy* **6**, 288–289
567 (2010).
- 568 25. Tumbarello, D. A. *et al.* The Autophagy Receptor TAX1BP1 and the Molecular Motor
569 Myosin VI Are Required for Clearance of Salmonella Typhimurium by Autophagy OPEN
570 ACCESS. *PLoS Pathog.* (2015). doi:10.1371/journal.ppat.1005174
- 571 26. Heo, J. M., Ordureau, A., Paulo, J. A., Rinehart, J. & Harper, J. W. The PINK1-PARKIN
572 Mitochondrial Ubiquitylation Pathway Drives a Program of OPTN/NDP52 Recruitment
573 and TBK1 Activation to Promote Mitophagy. *Mol. Cell* **60**, 7–20 (2015).
- 574 27. Wong, Y. C. & Holzbaur, E. L. F. Optineurin is an autophagy receptor for damaged
575 mitochondria in parkin-mediated mitophagy that is disrupted by an ALS-linked mutation.
576 *Proc. Natl. Acad. Sci.* **111**, E4439–E4448 (2014).
- 577 28. Lu, K., Psakhye, I. & Jentsch, S. Autophagic Clearance of PolyQ Proteins Mediated by
578 Ubiquitin-Atg8 Adaptors of the Conserved CUET Protein Family. (2014).
579 doi:10.1016/j.cell.2014.05.048
- 580 29. Lamark, T., Kirkin, V., Dikic, I. & Johansen, T. NBR1 and p62 as cargo receptors for
581 selective autophagy of ubiquitinated targets. *Cell Cycle* **8**, 1986–1990 (2009).
- 582 30. Komatsu, M. *et al.* Homeostatic Levels of p62 Control Cytoplasmic Inclusion Body
583 Formation in Autophagy-Deficient Mice. *Cell* **131**, 1149–1163 (2007).
- 584 31. Eggers, D. K., Welch, W. J. & Hansen, W. J. Complexes between nascent polypeptides
585 and their molecular chaperones in the cytosol of mammalian cells. *Mol. Biol. Cell* **8**,
586 1559–73 (1997).
- 587 32. Yewdell, J. W., Antón, L. C. & Bennink, J. R. Defective ribosomal products (DRiPs): a

- 588 major source of antigenic peptides for MHC class I molecules? **157**, 1823–1826 (1996).
- 589 33. Kirkin, V., Lamark, T., Johansen, T. & Dikic, I. NBR1 cooperates with p62 in selective
590 autophagy of ubiquitinated targets. *Autophagy* **5**, 732–733 (2009).
- 591 34. Bjørkøy, G. *et al.* p62/SQSTM1 forms protein aggregates degraded by autophagy and has
592 a protective effect on huntingtin-induced cell death. *J. Cell Biol.* **171**, 603–614 (2005).
- 593 35. Wang, C. *et al.* Scalable Production of iPSC-Derived Human Neurons to Identify Tau-
594 Lowering Compounds by High-Content Screening. *Stem Cell Reports* **9**, 1221–1233
595 (2017).
- 596 36. Yang, Y., Wang, G., Huang, X. & Du, Z. Structural Biology Communications Expression,
597 purification and crystallization of the SKICH domain of human TAX1BP1. *Cryst.*
598 *Commun. Acta Cryst* **70**, 619–623 (2014).
- 599 37. Wang, D. B., Gitcho, M. A., Kraemer, B. C. & Klein, R. L. Genetic strategies to study
600 TDP-43 in rodents and to develop preclinical therapeutics for amyotrophic lateral
601 sclerosis. *Eur. J. Neurosci.* **34**, 1179–1188 (2011).
- 602 38. Liachko, N. F., Guthrie, C. R. & Kraemer, B. C. Neurobiology of Disease
603 Phosphorylation Promotes Neurotoxicity in a *Caenorhabditis elegans* Model of TDP-43
604 Proteinopathy. (2010). doi:10.1523/JNEUROSCI.2911-10.2010
- 605 39. Johnson, B. S., Mccaffery, J. M., Lindquist, S. & Gitler, A. D. *A yeast TDP-43*
606 *proteinopathy model: Exploring the molecular determinants of TDP-43 aggregation and*
607 *cellular toxicity.* (2008).
- 608 40. Barmada, S. J. *et al.* Cytoplasmic Mislocalization of TDP-43 Is Toxic to Neurons and
609 Enhanced by a Mutation Associated with Familial Amyotrophic Lateral Sclerosis. (2010).
610 doi:10.1523/JNEUROSCI.4988-09.2010
- 611 41. Wils, H. *et al.* TDP-43 transgenic mice develop spastic paralysis and neuronal inclusions

- 612 characteristic of ALS and frontotemporal lobar degeneration.
613 doi:10.1073/pnas.0912417107
- 614 42. Ravikumar, B., Duden, R. & Rubinsztein, D. C. Aggregate-prone proteins with
615 polyglutamine and polyalanine expansions are degraded by autophagy. *Hum. Mol. Genet.*
616 **11**, 1107–17 (2002).
- 617 43. Iwata, A. *et al.* Increased susceptibility of cytoplasmic over nuclear polyglutamine
618 aggregates to autophagic degradation. (2005).
- 619 44. Krobitch, S. & Lindquist, S. *Aggregation of huntingtin in yeast varies with the length of*
620 *the polyglutamine expansion and the expression of chaperone proteins.* (1999).
- 621 45. Yamamoto, A. & Simonsen, A. The elimination of accumulated and aggregated proteins:
622 A role for aggrephagy in neurodegeneration. (2010). doi:10.1016/j.nbd.2010.08.015
- 623 46. Menzies, F. M., Moreau, K. & Rubinsztein, D. C. Protein misfolding disorders and
624 macroautophagy. *Curr. Opin. Cell Biol.* **23**, 190–7 (2011).
- 625 47. Rose, C. *et al.* Rilmenidine attenuates toxicity of polyglutamine expansions in a mouse
626 model of Huntington’s disease. doi:10.1093/hmg/ddq093
- 627 48. Sarkar, S., Davies, J. E., Huang, Z., Tunnacliffe, A. & Rubinsztein, D. C. Trehalose, a
628 Novel mTOR-independent Autophagy Enhancer, Accelerates the Clearance of Mutant
629 Huntingtin and-Synuclein * □ S. (2007). doi:10.1074/jbc.M609532200
- 630 49. Brumell, J. H., Cemma, M., Kim, P. K. & Brumell, J. H. The ubiquitin-binding adaptor
631 proteins p62/SQSTM1 and NDP52 are recruited independently to bacteria-associated
632 microdomains to target Salmonella to the autophagy pathway. *Autophagy* **341** *Autophagy*
633 **7**, 5909–5925 (2011).
- 634 50. Yang, Y., Wang, G., Huang, X. & Du, Z. Crystallographic and modelling studies suggest
635 that the SKICH domains from different protein families share a common Ig-like fold but

- 636 harbour substantial structural variations. *J. Biomol. Struct. Dyn.* **33**, 1385–1398 (2015).
- 637 51. Shembade, N., Harhaj, N. S., Liebl, D. J. & Harhaj, E. W. Essential role for TAX1BP1 in
638 the termination of TNF- α , IL-1-and LPS-mediated NF- κ B and JNK signaling. *EMBO J.*
639 **26**, 3910–3922 (2007).
- 640 52. Shembade, N., Pujari, R., Harhaj, N. S., Abbott, D. W. & Harhaj, E. W. The kinase IKK α
641 inhibits activation of the transcription factor NF- κ B by phosphorylating the regulatory
642 molecule TAX1BP1. (2011). doi:10.1038/ni.2066
- 643 53. Choi, A. J. S. & Ryter, S. W. Review Article Autophagy in Inflammatory Diseases. *Int. J.*
644 *Cell Biol.* **2011**, 11 (2011).
- 645 54. Lim, J. & Yue, Z. Developmental Cell Review Neuronal Aggregates: Formation,
646 Clearance, and Spreading. *Dev. Cell* **32**, 491–501 (2015).
- 647 55. Czirr, E. & Wyss-Coray, T. The immunology of neurodegeneration. *J. Clin. Invest.* **122**,
648 1156–63 (2012).
- 649 56. Carpenter, A. E. *et al.* CellProfiler: image analysis software for identifying and
650 quantifying cell phenotypes. *Genome Biol.* (2006). doi:10.1186/gb-2006-7-10-r100
- 651 57. Pau, G., Fuchs, F., Sklyar, O., Boutros, M. & Huber, W. EBImage-an R package for
652 image processing with applications to cellular phenotypes. *Bioinformatics* (2010).
653 doi:10.1093/bioinformatics/btq046
- 654 58. Ritz, C., Baty, F., Streibig, J. C. & Gerhard, D. Dose-response analysis using R. *PLoS One*
655 (2015). doi:10.1371/journal.pone.0146021
- 656 59. He, Z., Xu, X., Huang, J. Z. & Deng, S. *FP-Outlier: Frequent Pattern Based Outlier*
657 *Detection.*
- 658
- 659

660 **Figure Legends**

661 **Figure 1. TAX1BP1 depletion impairs clearance of protein aggregates.** **a**, Validation of
662 knockout cell lines. **b**, Experimental outline for assessing aggregate formation and clearance. **c**,
663 WT or individual knockouts for p62, NBR1, NDP52, OPTN, and TAX1BP1 cell lines were
664 exposed to 5 $\mu\text{g/ml}$ puromycin for 2 h, after which cells were either fixed for imaging or washed
665 and followed for a further 3 h in full media; scale bar 10 μm . **d, f**, Quantification of **b**: percent of
666 cells containing UB-positive foci was assessed in ~ 200 cells per condition in 3 independent
667 experiments at (d) 2 h puromycin or (f) 2 h puromycin followed by 3 h washout. Quantification is
668 displayed as mean \pm s.d. from 3 independent experiments using one-way ANOVA test (** $P < 0.01$,
669 *** $P < 0.001$, **** $P < 0.0001$) comparing all to WT and Tukey's post hoc test. **e, g**, WT normalized
670 comparisons of foci formation and foci clearance in autophagy receptor knockout cell lines. **h**,
671 WT, pentaKO, or individual KO lines for each autophagy receptor were treated with 1 μM MG132
672 for 8 or 18 h, fractionated into RIPA-soluble or -insoluble fractions and immunoblotted for total
673 ubiquitin. Quantification and soluble fractions shown in Supp. Fig. 1C and 1D, respectively. **i**, WT
674 or TAX1BP1 KO cell lines were exposed to 100 nM Bafilomycin A or 1 μM MG132 for 5 h then
675 fixed for imaging. **j**, Quantification of **i**: percent of cells containing UB-positive foci was assessed
676 in ~ 200 cells per condition. Quantification is displayed as mean \pm s.d. from 3 independent
677 experiments using one-way ANOVA test, (**** $P < 0.0001$) comparing all to WT and Tukey's post
678 hoc test. The number of observations used in each experimental series and P values for all
679 comparisons are included in Table 1. All blots and microscopy images are representative of at least
680 3 independent experiments.

681

682 **Figure 2. TAX1BP1 protein responds to proteotoxic stress and associates with insoluble**
683 **protein.** **a, b**, WT HeLa cells were treated with either (a) puromycin or (b) MG132 as indicated,

684 lysed in 2% SDS and immunoblotted for TAX1BP1, OPTN, NBR1, p62, or NDP52. **c**, WT cells
685 treated with 1 μ M MG132 for 8 or 18 h were fractionated into RIPA-soluble or -insoluble
686 fractions and immunoblotted for TAX1BP1. **d**, Human tissue panel probed for TAX1BP1 or
687 NDP52. **e**, Primary rat cortical neurons were treated with the indicated amounts of MG132 for 8
688 or 18 h, fractionated into RIPA-soluble or -insoluble fractions and immunoblotted for total UB. **f**,
689 Fractionated primary rat cortical neurons treated as in (e) were blotted for the indicated proteins.
690 All blots are representative of at least 3 independent experiments.

691
692 **Figure 3. TAX1BP1 mediates aggregate clearance.** **a**, WT, TAX1BP1 KO, and TAX1BP1 KO
693 with stable expression of GFP-TAX1BP1 rescue cell lines were exposed to 5 μ g/ml puromycin
694 for 2 h, after which cells were either fixed for imaging or washed and followed for a further 3 h
695 in full media; scale bar 10 μ m. **b**, Quantification of (a): percent of cells containing UB-positive
696 foci was assessed in \sim 200 cells per condition. Quantification is displayed as mean \pm s.d. from 3
697 independent experiments using one-way ANOVA test (**** P <0.0001) and Tukey's post hoc
698 test. **c**, **d**, Stably-expressing TAX1BP1 rescue lines were created using either N-FLAG or C-
699 FLAG tag at high (H) or low (L) expression levels (See Supplementary Figure 3A, 3B) and
700 exposed to 5 μ g/ml puromycin for 2 h, after which cells were either fixed for imaging (c) or
701 washed and followed for a further 3 h in full media (d) and quantified as in (b). **e**, WT,
702 TAX1BP1 KO, or TAX1BP1 KO + FLAG-TAX1BP1 (H) cell lines were exposed to 5 μ g/ml
703 puromycin in the presence or absence of 100 nM Bafilomycin A, after which cells were either
704 fixed for imaging or washed and followed for a further 3 h in full media or in full media
705 containing Bafilomycin A. Larger fields of view shown in Supplementary Figure 3C. **f**,
706 Quantification of e: percent of cells containing UB-positive foci was assessed in \sim 200 cells per
707 condition in 3 independent experiments. Quantification is displayed as mean \pm s.d. from 3

708 independent experiments using two-way ANOVA test, (**** $P < 0.0001$). The number of
709 observations used in each experimental series and P values for all comparisons are included in
710 Table 1. All images are representative of at least 3 independent experiments.
711
712 **Figure 4. Requirements for TAX1BP1 domains in aggregophagy** **a**, TAX1BP1 truncation or
713 point mutations used in this study. **b, i-x**, TAX1BP1 KO and TAX1BP1 KO with stable
714 expression of TAX1BP1 mutants were exposed to 5 $\mu\text{g/ml}$ puromycin for 2 h, after which cells
715 were either fixed for imaging or washed and followed for a further 3 h in full media; scale bar
716 10 μm , larger fields of view shown in Supplementary Figure 4A. **c**, Quantification of UB-foci
717 formation observed in (b). **d**, Quantification of UB-foci clearance observed in (b), percent of
718 cells containing UB-positive foci was assessed in ~ 200 cells per condition. **e**, Quantification of
719 UB-foci formation observed in TKO (OPTN/NDP52/TAX1BP1). See Supplementary Figure 4C
720 for images. **f**, Quantification of UB-foci clearance observed in TKO. See Supplementary Figure
721 4C for images, percent of cells containing UB-positive foci was assessed in ~ 200 cells per
722 condition. **g**, WT cells stably expressing high levels of FLAG-TAX1BP1 were exposed to 5
723 $\mu\text{g/ml}$ puromycin for 2 h, after which cells were either fixed for imaging or washed and followed
724 for a further 3 h in full media; scale bar 10 μm . **h**, Quantification of UB-foci formation observed
725 in (g) and in Supplementary Figure 4D. **i**, Quantification of UB-foci clearance observed in (g)
726 and in Supplementary Figure 4D, percent of cells containing UB-positive foci was assessed in \sim
727 200 cells per condition. All quantification is displayed as mean \pm s.d. from 3 independent
728 experiments using one-way ANOVA test comparing all to WT ($*P < 0.05$, $**P < 0.01$,
729 $***P < 0.001$, $****P < 0.0001$) and Tukey's post hoc test. The number of observations used in
730 each experimental series and P values for all comparisons are included in Table 1. All images are
731 representative of at least 3 independent experiments.

732

733 **Figure 5. TAX1BP1 mediates aggregophagy of cytotoxic aggregation-prone proteins. a, WT,**
734 TAX1BP1 knockout, or TAX1BP1 knockout with stably-expressed TAX1BP1 rescue cell lines
735 were exposed to proteotoxic stressors as indicated on Day 1, then followed for 6 days during
736 which viability was measured by quantification of ATP production. Relative viability represents
737 normalized luminescence displayed as mean \pm s.d. from 3 independent experiments; significance
738 was assessed using two-way ANOVA test (**** $P < 0.0001$, *** $P < 0.001$, ** $P < 0.01$, * $P < 0.05$)
739 with Tukey's post hoc test. P values and normalized viability measurements shown on graphs are
740 for day 6 comparisons. The individual measurements for each time point and conditions used in
741 each experimental series and P values for all comparisons are included in Table 1. **b, WT,**
742 TAX1BP1 knockout, or rescue cells uninfected or infected with virus expressing HttQ23-EGFP,
743 HttQ74-EGFP, or HttQ103-EGFP were assessed 4 days post-infection. **c, Quantification of**
744 HttQ74-EGFP aggregates observed in (b), **d, Quantification of HttQ103-EGFP aggregates**
745 observed in (b), percent of cells containing GFP-positive foci was assessed in ~ 200 cells per
746 condition in 3 independent experiments. Quantification is displayed as mean \pm s.d. from 3
747 independent experiments using one-way ANOVA test (** $P < 0.01$, *** $P < 0.001$, **** $P < 0.0001$)
748 and Tukey's post hoc test. The number of observations used in each experimental series is
749 included in Table 1. All images are representative of at least 3 independent experiments. **e,**
750 Immunofluorescence labeling of endogenous TAX1BP1 in cells infected with HttQ23-EGFP or
751 HttQ103-EGFP. Maximum intensity projections shown. **f, A single 1 μ m slice is shown from**
752 images taken of immunofluorescence labeling of endogenous TAX1BP1 in cells infected with
753 HttQ103-EGFP as in (e). Scale bars 10 μ m. **g, h, Graphs show line fitted to the number of BFP-**
754 **positive nuclei counted daily for iPSC-derived neurons with or without stable TAX1BP1**
755 **overexpression infected with HttQ23-EGFP (g) or HttQ103-EGFP (h). Ribbon represents 95%**

756 confidence interval around the fitted line. Beeswarm box plots compare survival scores
757 determined by performing permutation analysis using the means of all slopes (center line =
758 median, box limits = first to third quartile, whiskers = minimum and maximum). The number of
759 observations used in each experimental series is included in Table 2.

760 **Supplementary Figure Legends**

761 **Supplementary Figure 1. a**, Schematic illustration of protein domain architectures of
762 mammalian autophagy receptors OPTN, NDP52, TAX1BP1, p62, and NBR1. PB1, Phox and
763 Bem1 domain; ZZ, ZZ-type zinc finger domain; NLS1 and NLS2, nuclear localization signals 1
764 and 2; NES, nuclear export signal; LIR, LC3-interacting region; KIR, Keap-interacting region;
765 UBA, ubiquitin-associated domain; CC, coiled-coil domain; FW, four tryptophan domain;
766 SKICH, SKIP carboxyl homology domain; ZF, Zinc-finger domain; UBAN ubiquitin binding in
767 ABIN and NEMO domain. The size of the receptors (in number of amino acids) is indicated. **b**,
768 Representative image of segmentation analysis performed using CellProfiler. **c, d**, Quantification
769 of (b) using CellProfiler: number of foci per cell in WT or TAX1BP1 KO cells in 3 independent
770 experiments at (c) 2 h puromycin or (d) 2 h puromycin followed by 3 h washout (For box plots,
771 center line = median, box limits = first to third quartile, whiskers = minimum and maximum). **e**,
772 WT and individual knockouts for p62, NBR1, NDP52, OPTN, and TAX1BP1 cell lines were
773 exposed to 1 μ M MG132 for 8 or 18 h, after which cells were either fixed for imaging or washed
774 and followed for a further 3 h in full media; scale bar 10 μ m. **f**, Quantification of Figure 1H
775 determined by densitometry and normalized first to soluble GAPDH and subsequently to WT
776 levels within each fraction. **g**, WT and individual KO lines for each autophagy receptor were
777 treated with 1 μ M MG132 for 8 or 18 h, fractionated into RIPA-soluble or -insoluble fractions
778 and immunoblotted for total UB. Soluble fractions shown here, insoluble fractions shown in
779 Figure 1H. All blots and microscopy images are representative of at least 3 independent
780 experiments.

781
782 **Supplementary Figure 2. a**, Primary rat cortical neurons treated with 1 μ M MG132 for 18 h,
783 after which cells were fixed for imaging and stained with antibodies for TAX1BP1 and UB;

784 scale bar 10 μ m. **b**, Neurons derived from human induced pluripotent stem cells (iPSCs) treated
785 with 1 μ M MG132 for 20 h, fixed and stained with antibodies targeting TAX1BP1 and UB; scale
786 bar 20 μ m. All images are representative of at least 3 independent experiments.

787

788 **Supplementary Figure 3. a**, GFP- or FLAG-tagged TAX1BP1 was stably reintroduced into
789 TAX1BP1 KO cells via viral infection. TAX1BP1 expression levels were titrated for use in
790 rescue experiments: L = low expression, H = high expression. **b**, Cell lines in (a) were exposed
791 to 5 μ g/ml puromycin for 2 h, after which cells were either fixed for imaging or washed and
792 followed for a further 3 h in full media; scale bar 10 μ m. **c**, Full field of view images associated
793 with Figure 3E, F showing WT, TAX1BP1 KO, or TAX1BP1 KO + FLAG-TAX1BP1 (H) cell
794 lines exposed to 5 μ g/ml puromycin in the presence or absence of 100 nM Bafilomycin A, after
795 which cells were either fixed for imaging or washed and followed for a further 3 h in full media
796 or in media containing Bafilomycin A. **d**, WT cells exposed to 5 μ g/ml puromycin for 2 h in the
797 presence or absence of Bafilomycin A, after which cells were either fixed for imaging or washed
798 and followed for a further 3 h in full media with or without Bafilomycin A; scale bar 10 μ m. All
799 images are representative of at least 3 independent experiments.

800

801 **Supplementary Figure 4. a**, Full field of view images of all TAX1BP1 stable mutant expression
802 cell lines exposed to 5 μ g/ml puromycin for 2 h, after which cells were either fixed for imaging
803 or washed and followed for a further 3 h in full media. Associated with Figure 4B, C, D. **b**,
804 Validation of knockout cell lines. **c**, TKO (triple knockout: TAX1BP1, OPTN, NDP52) cell line
805 with stable expression of TAX1BP1 mutants exposed to 5 μ g/ml puromycin after which cells
806 were either fixed for imaging or washed and followed for a further 3 h in full media; scale bar
807 10 μ m. **d**, WT cells stably expressing low levels of FLAG-TAX1BP1 were exposed to 5 μ g/ml

808 puromycin for 2 h, after which cells were either fixed for imaging or washed and followed for a
809 further 3 h in full media; scale bar 10 μ m. All images are representative of at least 3 independent
810 experiments.

811

812 **Supplementary Figure 5. a**, Constructs used in this study. **b**, Expression of GFP control or
813 GFP-TDP-43. **c**, WT, TAX1BP1 knockout, or TAX1BP1-rescue cells transfected with DNA
814 expressing EGFP-TDP-43 at the indicated concentrations on Day 1, then followed for 6 days
815 during which viability was measured by quantification of ATP production. Relative viability
816 represents normalized luminescence displayed as mean \pm s.d. from 3 independent experiments;
817 significance was assessed using two-way ANOVA test (**** P <0.0001, *** P <0.001, ** P <0.01)
818 with Tukey's post hoc test. P values and normalized viability measurements shown on graphs are
819 for day 6 comparisons. The individual measurements for each time point and conditions used in
820 each experimental series and P values for all comparisons are included in Table 1. **d**, A single
821 1 μ m slice is shown from images taken of immunofluorescence labeling of endogenous
822 TAX1BP1 in cells infected with HttQ103-EGFP; scale bar 10 μ m. **e**, Proteotoxic stress, induced
823 by translational stress, proteasome inhibition, or expression of aggregate-promoting proteins
824 causes misfolded or damaged proteins to assemble into toxic oligomers or aggregates. In WT
825 cells (green panel), the proteasome and aggrephagy both work to remove potentially toxic
826 protein products. If the proteasome is overwhelmed, aggregated protein is shunted to the
827 autophagy pathway. In the absence of TAX1BP1 (red panel), aggrephagy is deficient - once the
828 proteasome has become overwhelmed by misfolded or aggregated protein, there is decreased
829 backup clearance via aggrephagy, and insoluble protein accumulates, leading to toxicity and cell
830 death.

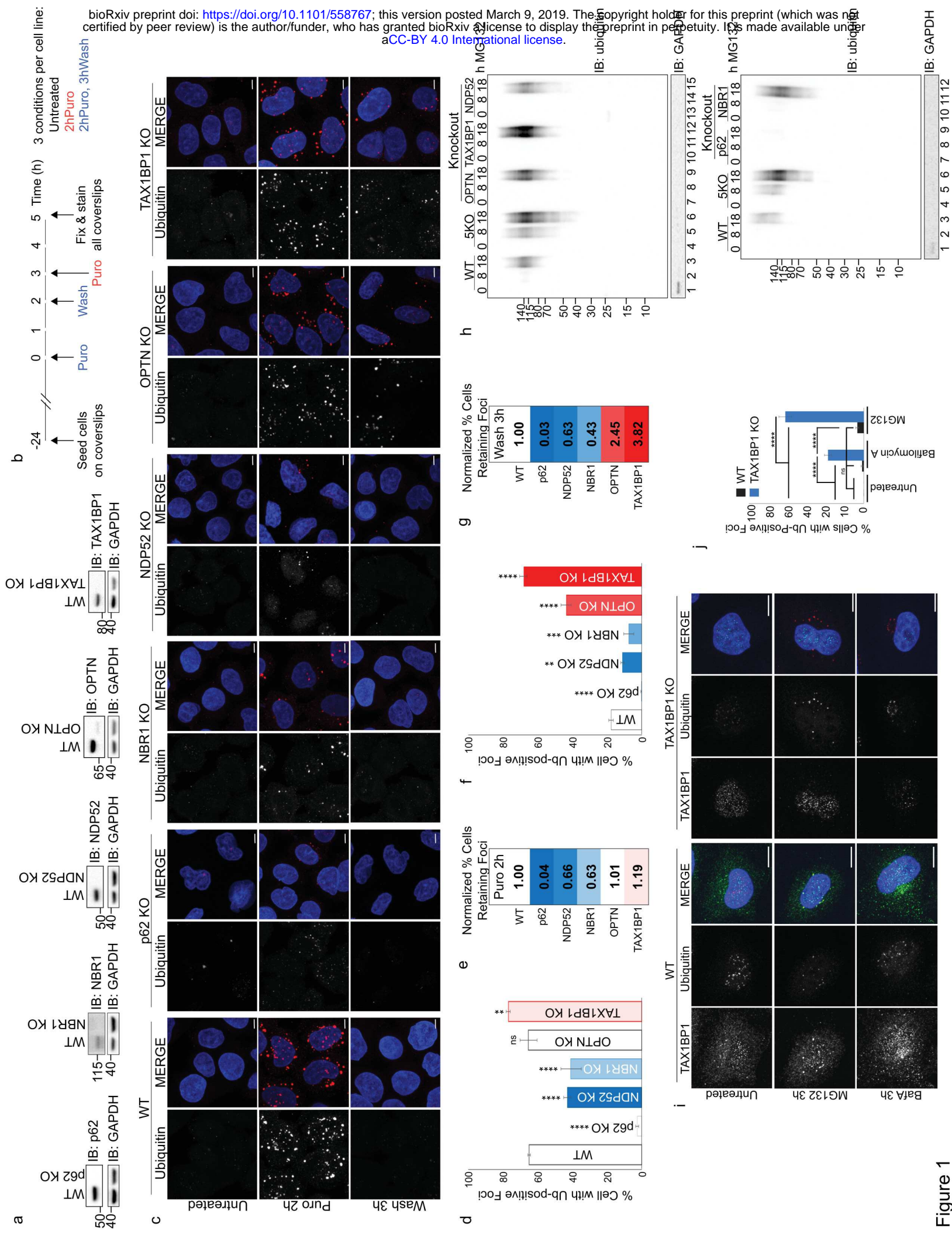


Figure 1

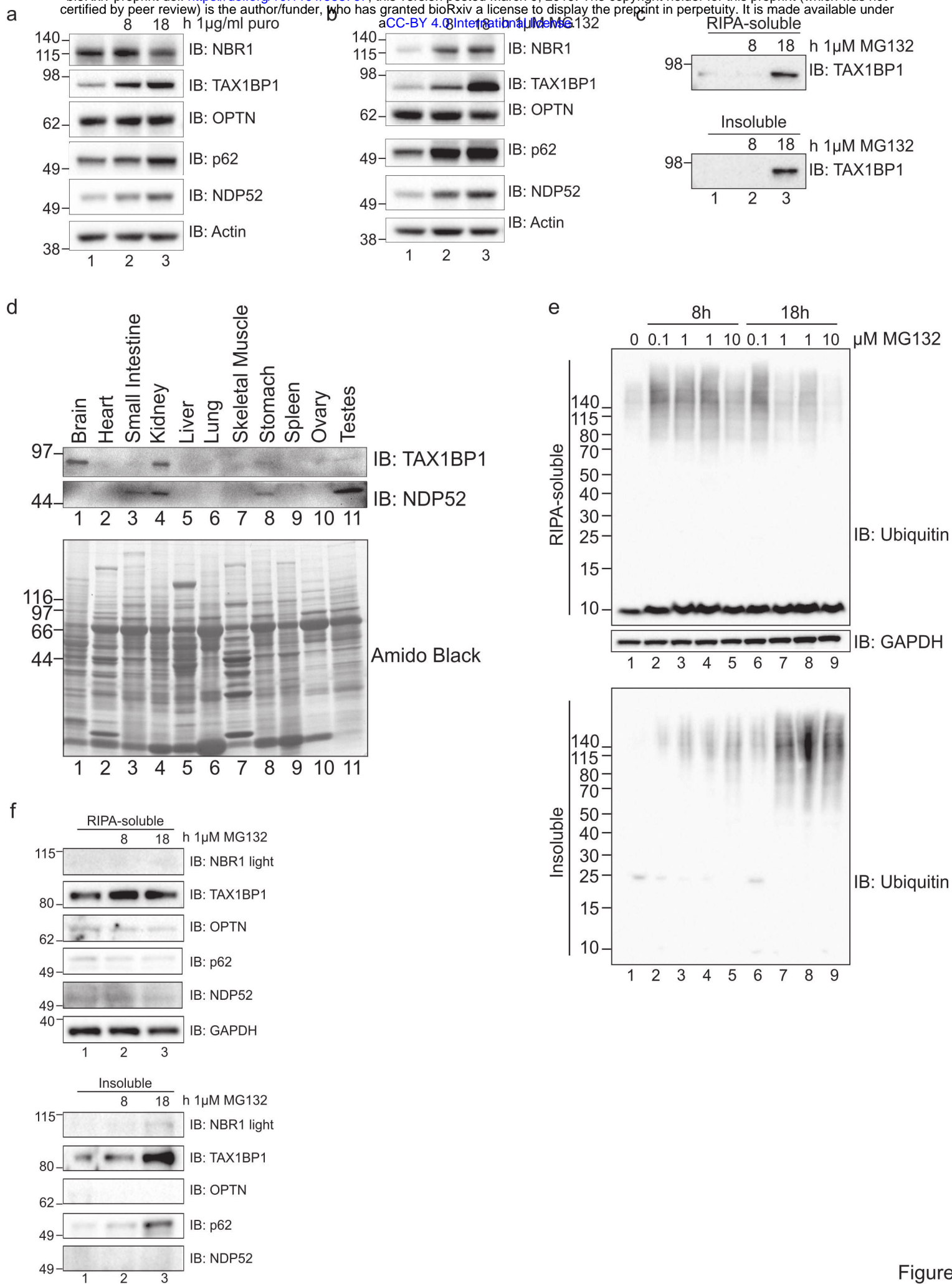


Figure 2

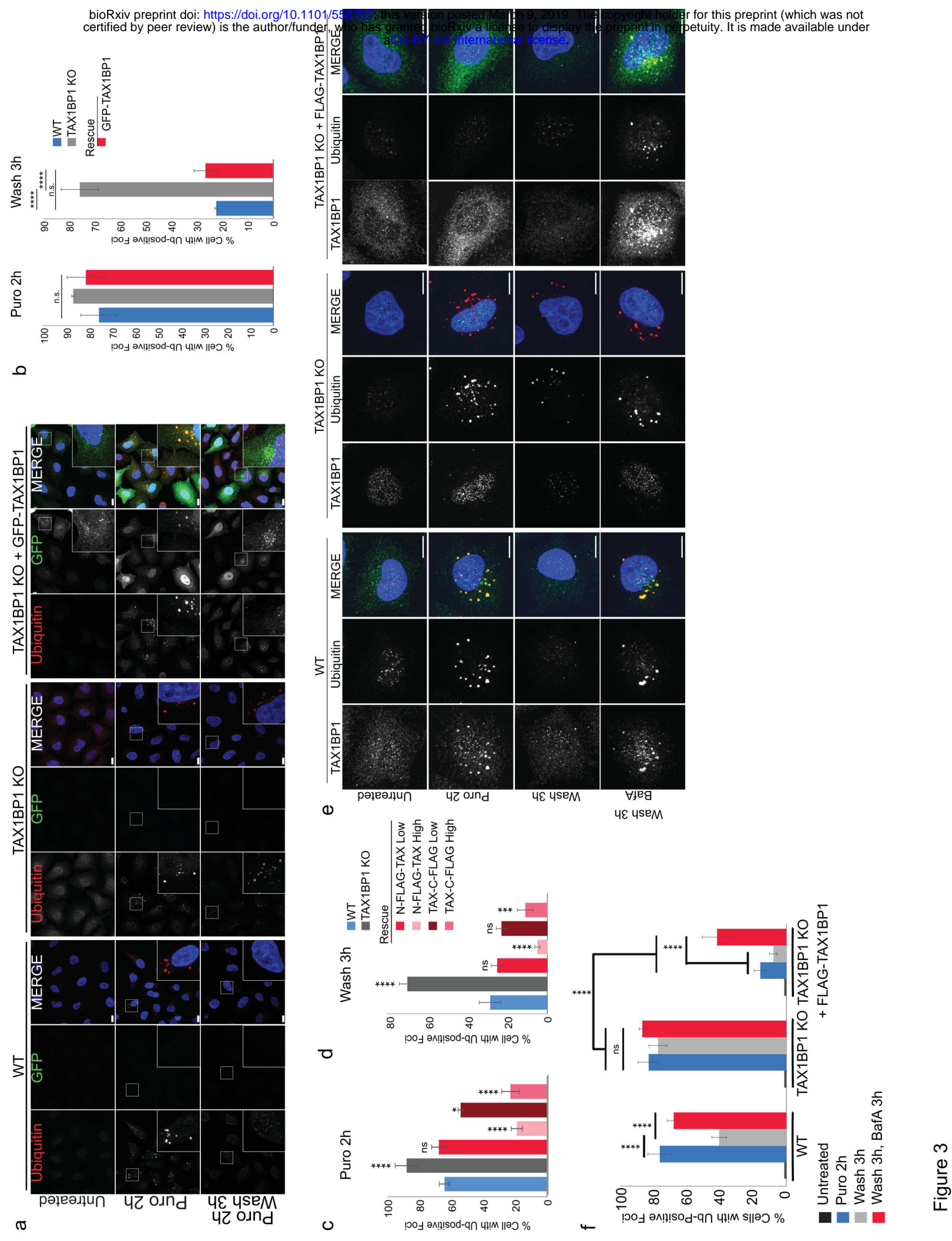
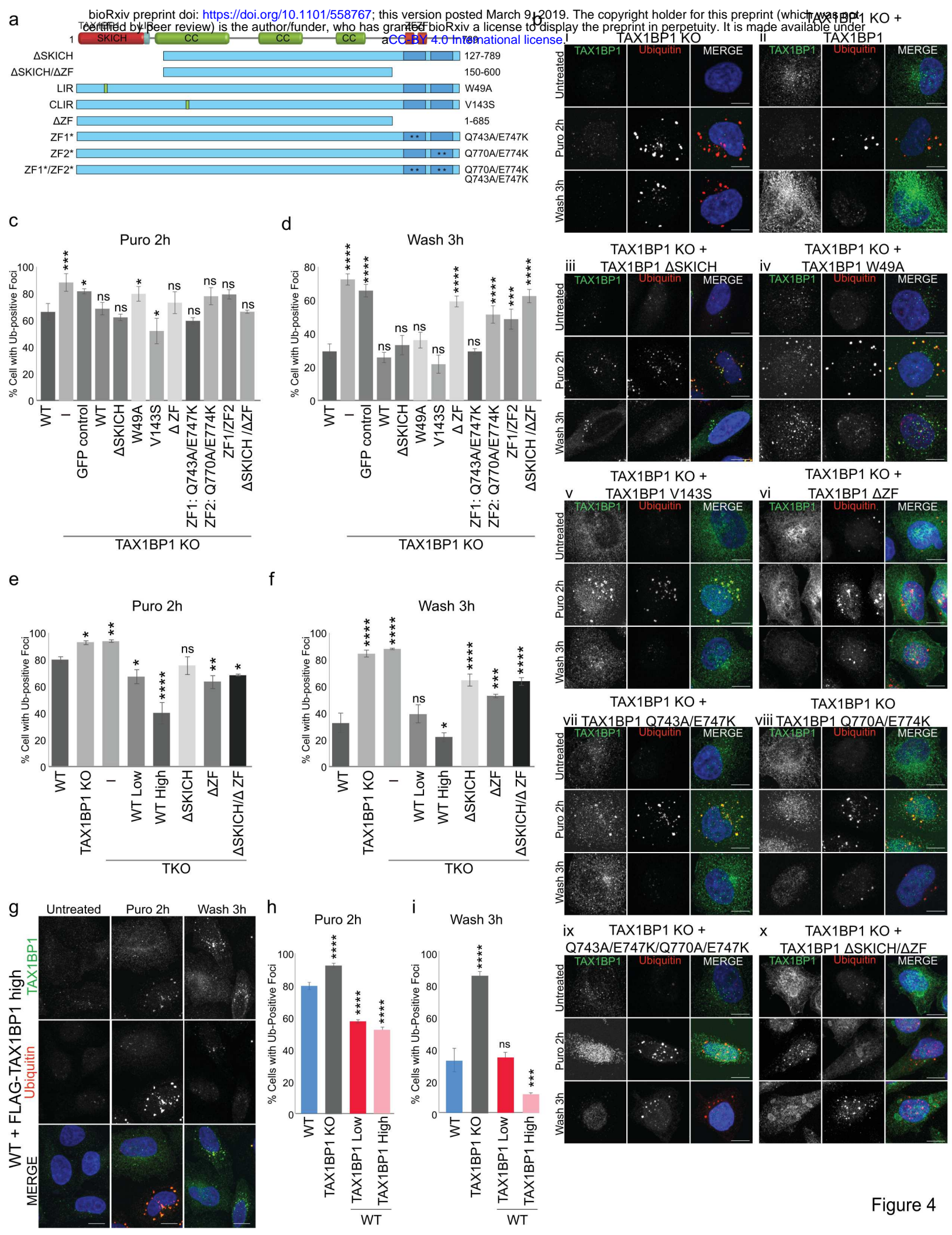
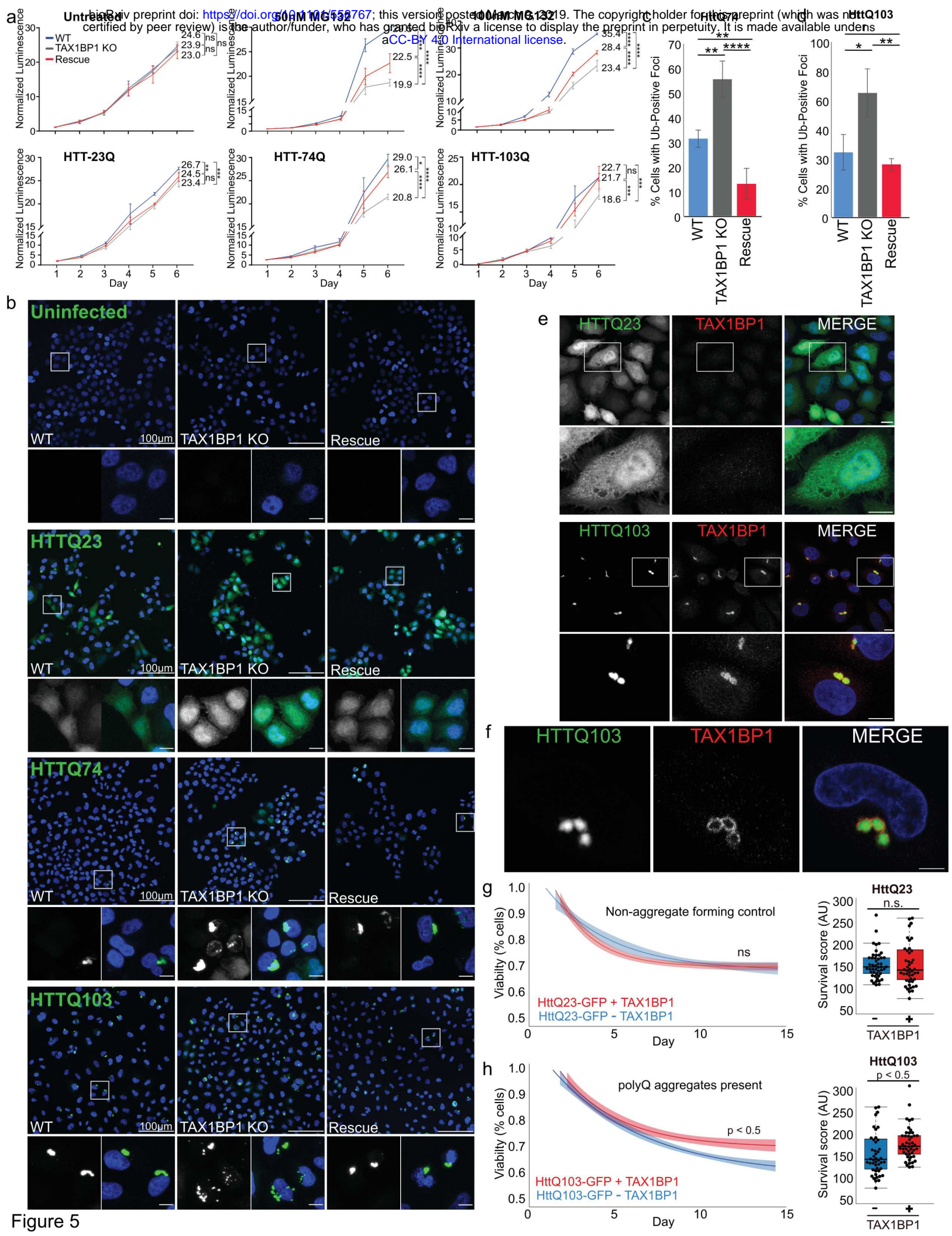
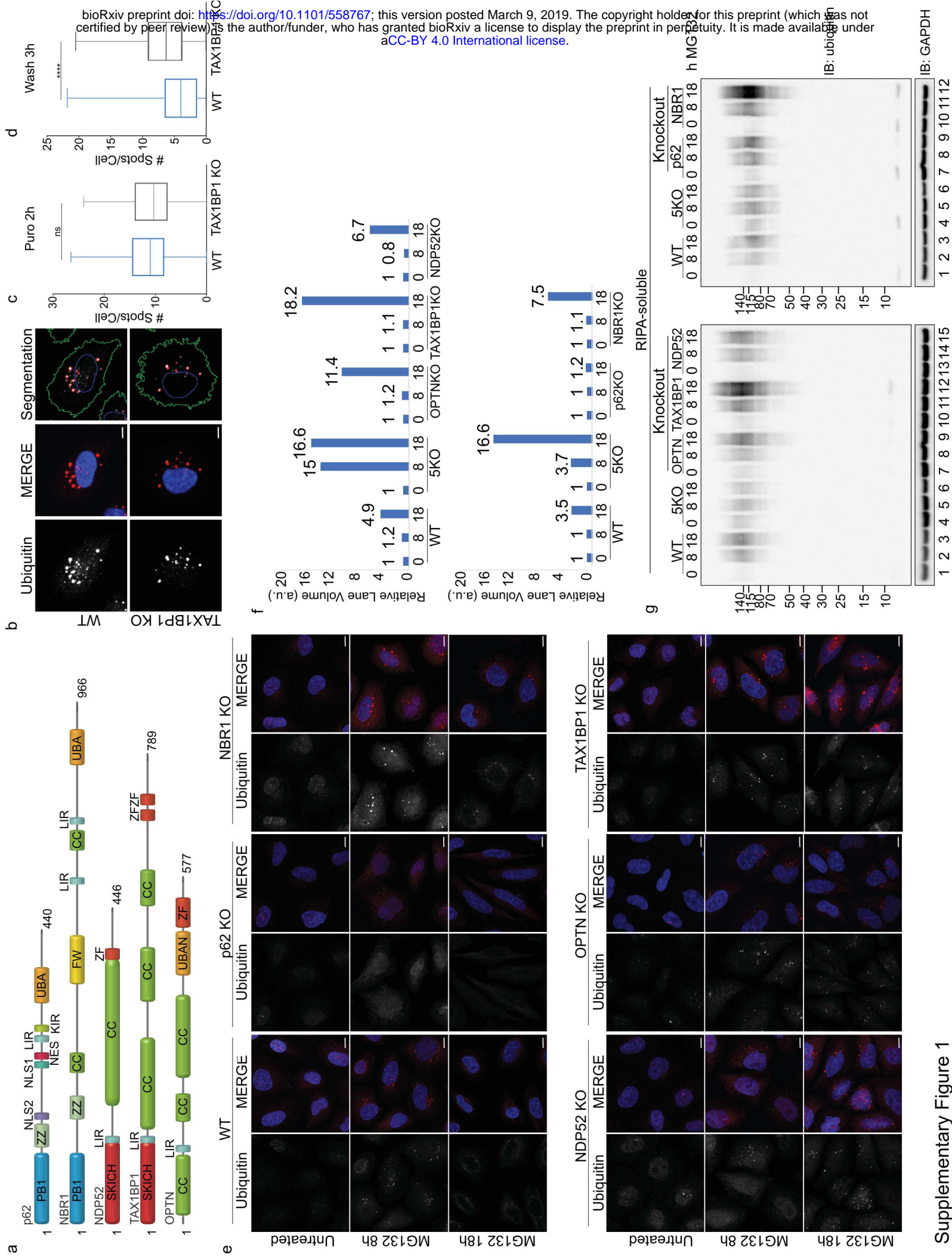


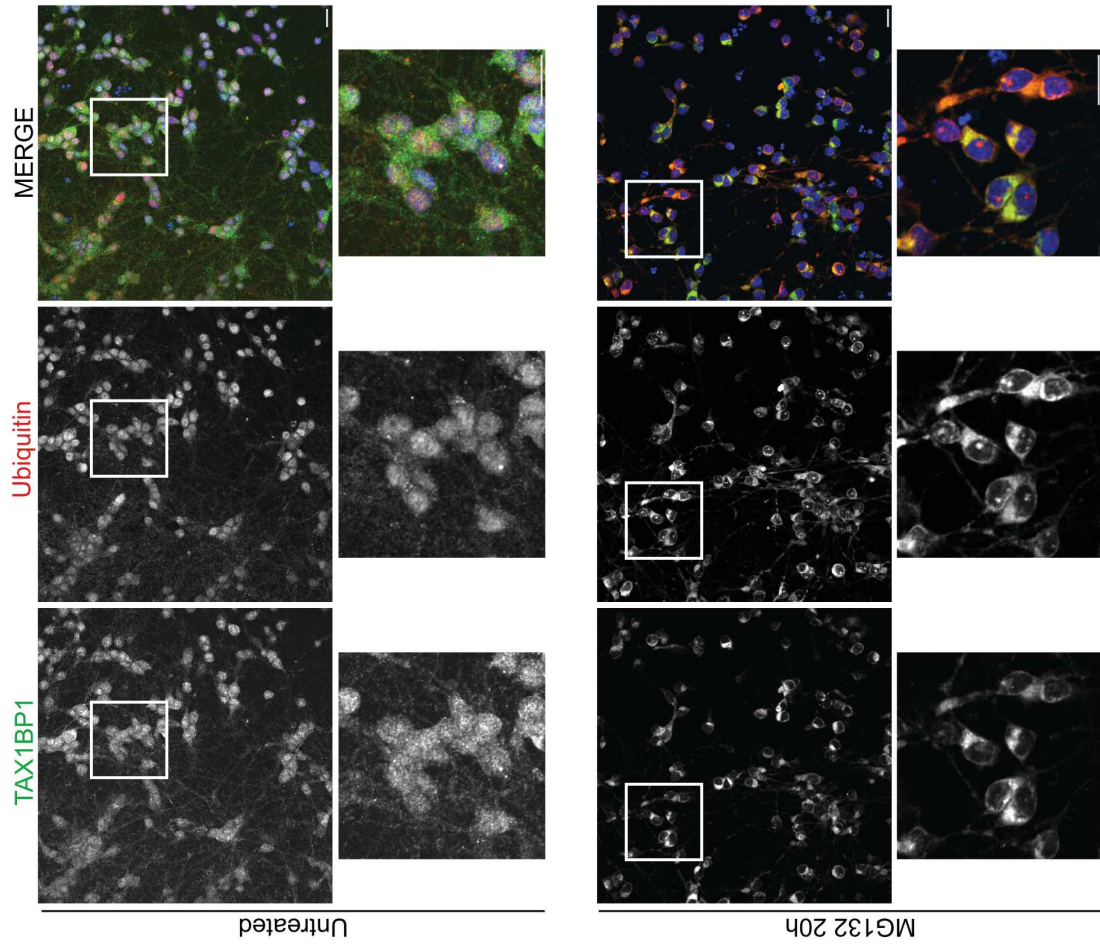
Figure 3



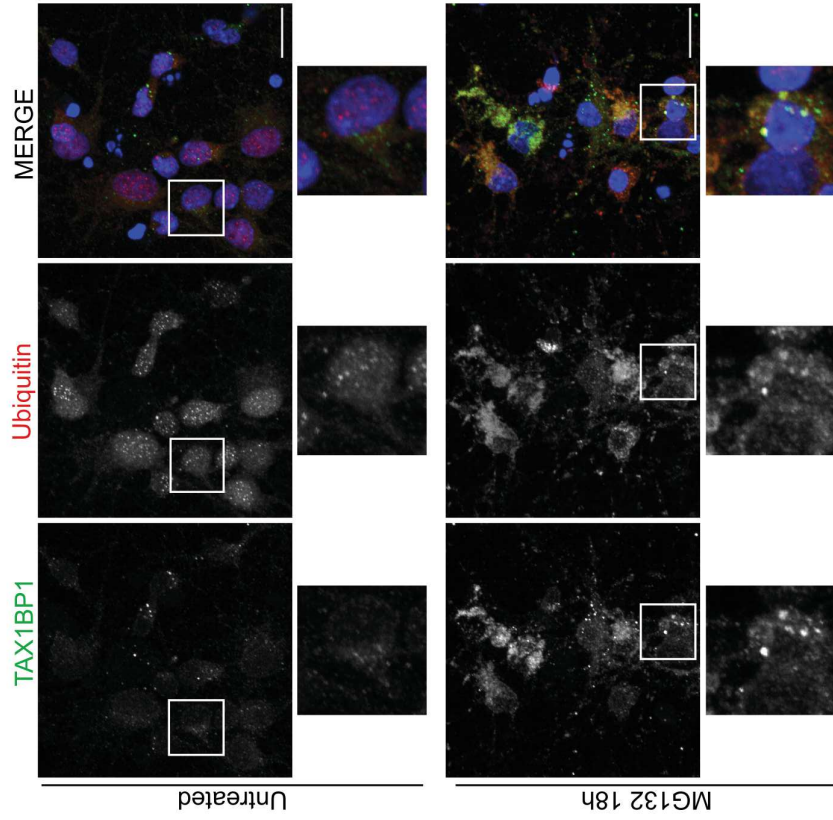


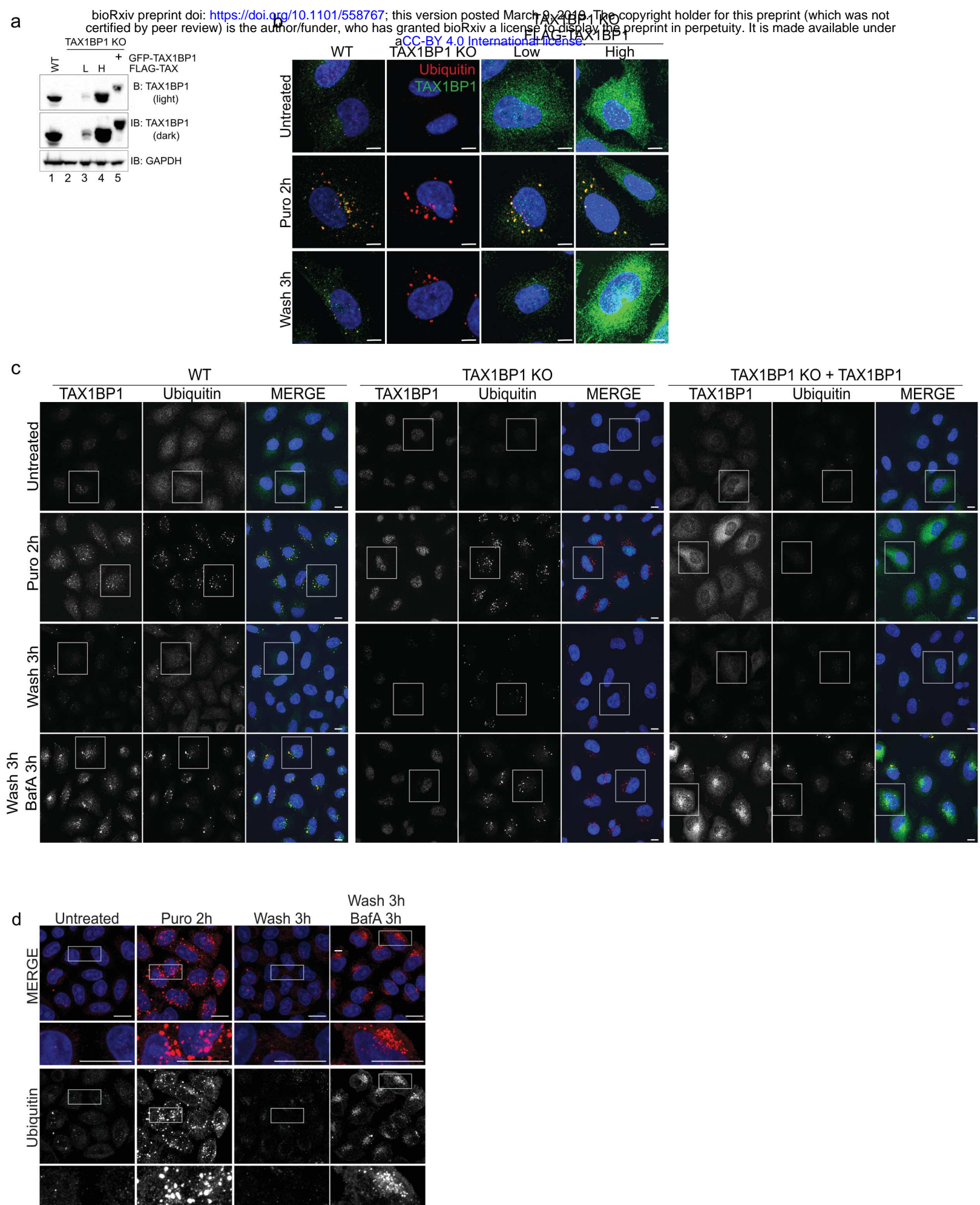


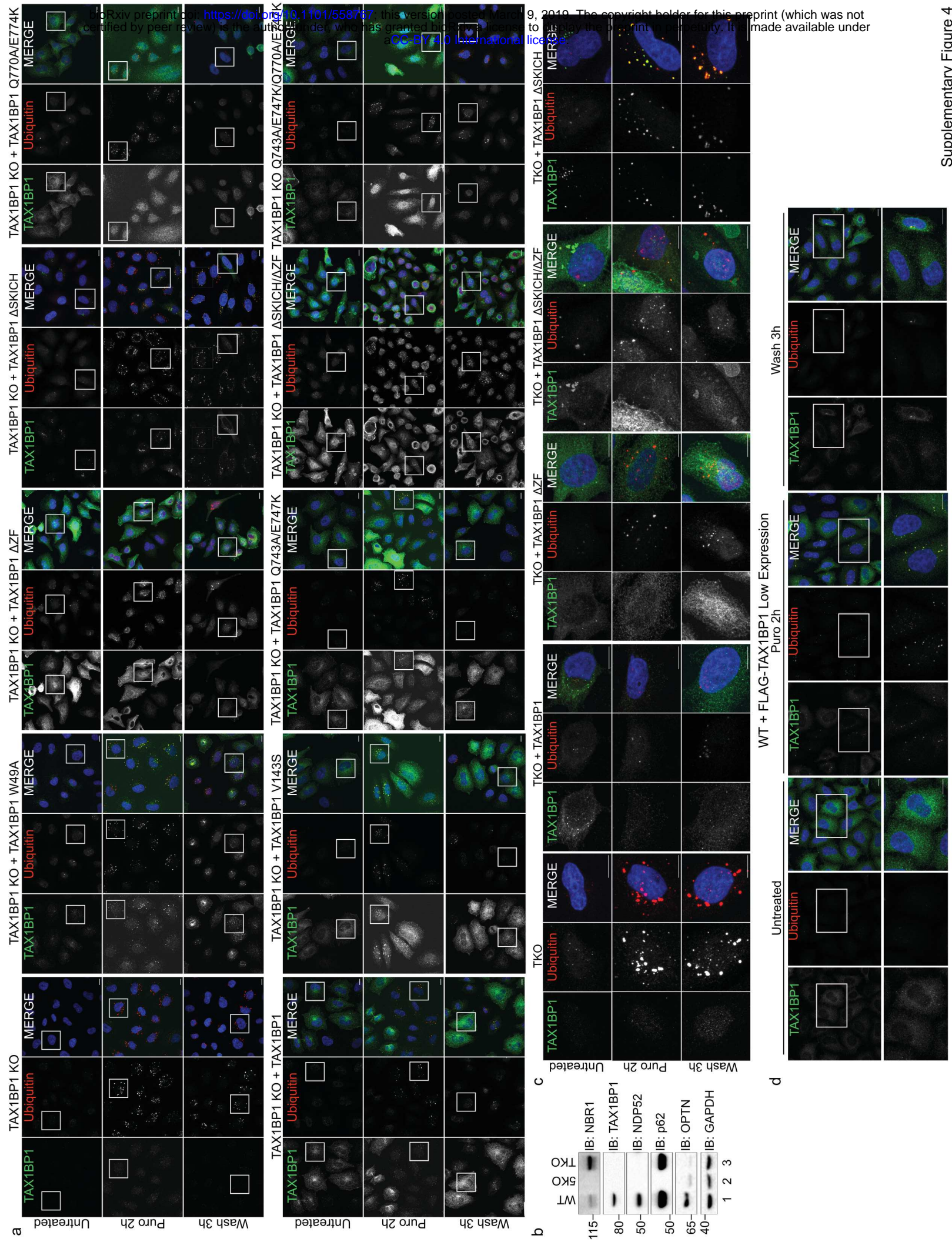
b



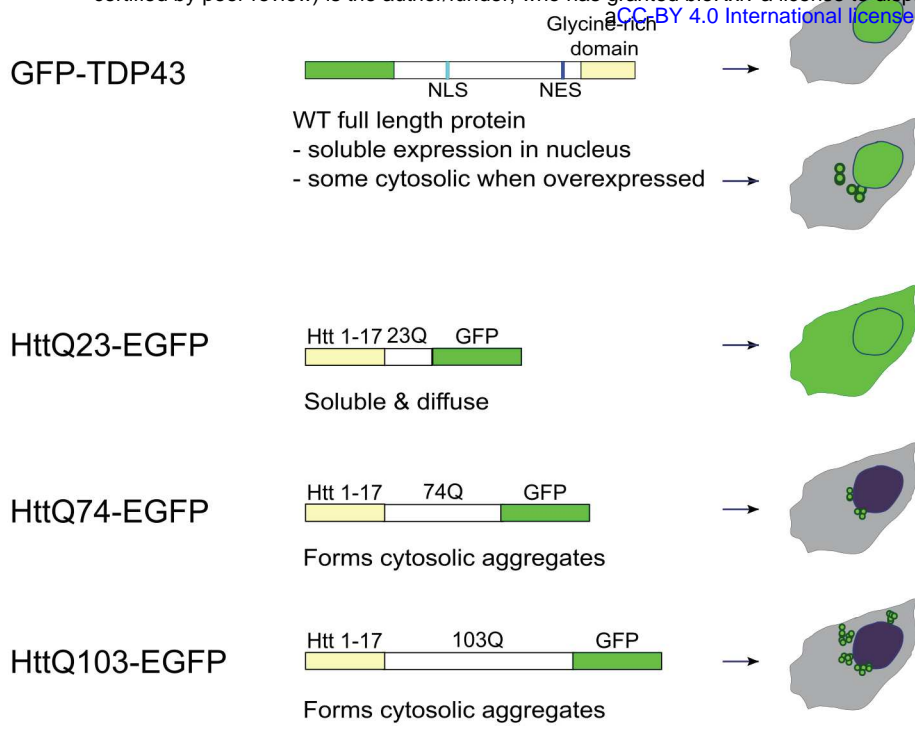
a



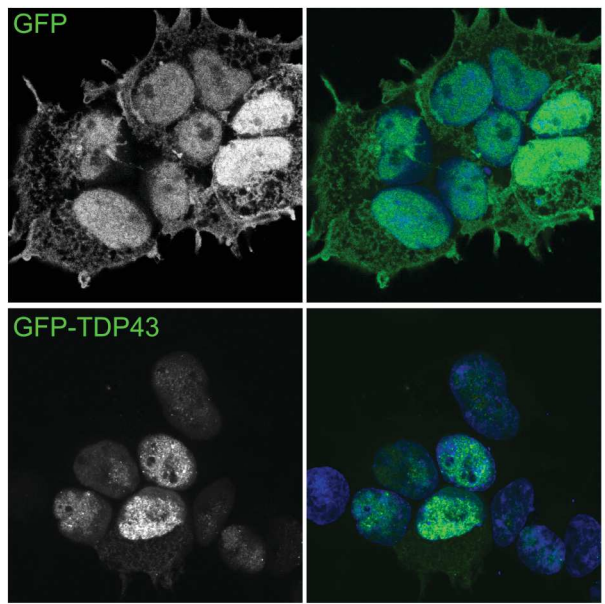




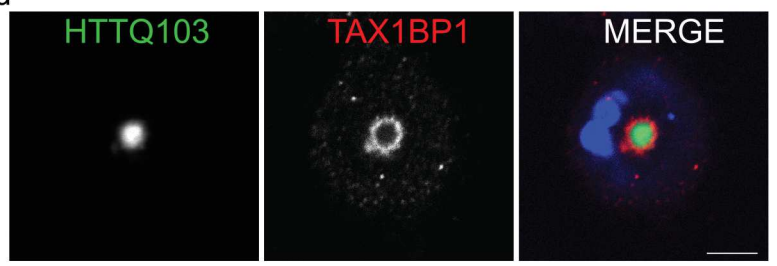
a



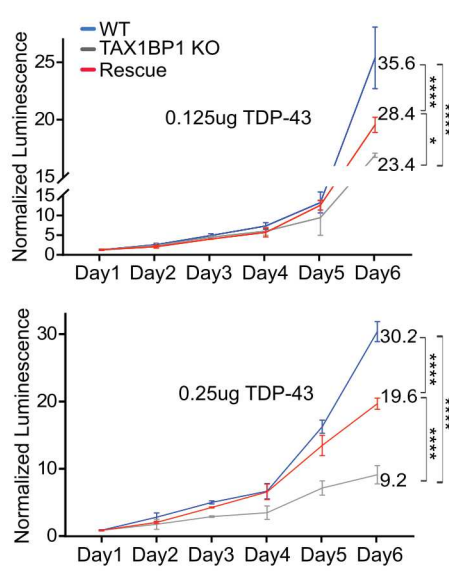
b



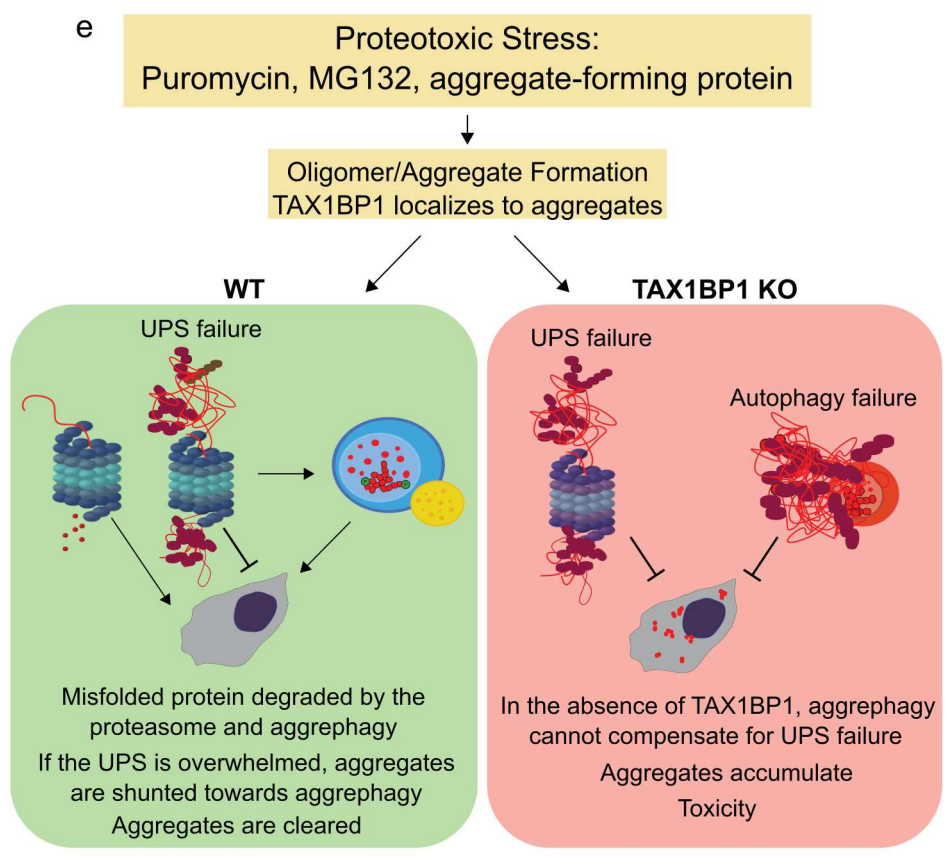
d



c



e



```
1 R code for Neuron Viability Analysis
2 ---
3 title: ""Selective autophagic clearance of protein aggregates is
4 mediated by the autophagy receptor, TAX1BP1""
5 output: html_notebook
6 ---
7 Images of the size 1200*1200 were segmented using the following
8 segmentation code.
9 ```{r}
10 args = (commandArgs(TRUE)) image.tif=args[1] library("dplyr")
11 library("data.table") library("gtools") library("EBImage")
12 library("outliers")
13 frame<-readImage(image.tif, type = "tif")
14 x<-1200
15 y<-1200
16 dapi<-frame[1:x,1:y,2] minDapi<-min(as.vector(dapi)) maxDapi<-
17 max(as.vector(dapi)) dapin<-normalize(dapi,
18 ft=c(0,1),c(minDapi,maxDapi)) dapi_normal<- dapin*(66)
19 nmask2 = thresh(dapi_normal, 50, 50,0.062) mk3 = makeBrush(11, shape=
20 "diamond") nmask2 = opening(nmask2, mk3)
21 nmask2 = fillHull(nmask2)
22 nseg = bwlabel(nmask2) #binery to object chackpoint<-
23 computeFeatures.shape(nseg) nmask = watershed(distmap(nmask2),1)
24 #display(nmask)
25 nf = computeFeatures.shape(nmask) nr = which(nf[,2] < 60)
26 nseg = rmObjects(nmask, nr) #display(nseg)
27 #rm(nf,nmask)
28 nn = max(nseg) chackpoint<-computeFeatures.shape(nseg) seg_GFP<-
29 paintObjects(nseg,toRGB(dapi*20),opac=c(1,
30 0.2),col=c("Green",NA),thick=F,closed=FALSE) chackpoint<-
31 computeFeatures.shape(nseg) df<-as.data.frame(chackpoint) xy<-
32 computeFeatures.moment(nseg)[,c('m.cx','m.cy')] df<-cbind(df,xy)
33 seg_GFP<-paintObjects(nseg,toRGB(dapi*20),opac=c(1,
34 0.2),col=c("Green",NA),thick=F,closed=FALSE) df.combine<-
35 as.data.frame(matrix(0,nrow(xy),5)) colnames(df.combine)<-
36 c("x","y","Area_real","Areal_roundess","ratio") df.combine$x<-xy[,1]
37 df.combine$y<-xy[,2] df.combine$Area_real<-df[,1] #area of sample
38 df.combine$Areal_roundess<-pi*(df[,3])^2 df.combine$ratio<-
39 df.combine[,4]/df[,1]
40 nr = which(df.combine[,5] > 1 )
41 gsegg = rmObjects(nseg, nr)
42 #rm(nseg,df)
43 nr = which(df.combine[,5] < 0.6 )
```



```
44 #rm(df.combine)
45 gsegg = rmObjects(gsegg, nr) bfp.number<-computeFeatures.shape(nseg)
46 seg_GFP<-paintObjects(gsegg,toRGB(dapi*60),opac=c(1,
47 0.2),col=c("Green",NA),thick=F,closed=FALSE)
48 #writeImage(seg_GFP,paste("processed",image.tif,sep = "_"))
49 write.table(nrow(bfp.number), file=args[2], row.names=FALSE, sep =
50 ";")
51 ```
52 The procedure was done on the nih biowulf server using the nih
53 parallel procedure unix command swarm.
54 swarm -g 16 --time 08:00:00 -f file.swarm --module R/3.5
55 Swarm file was creating by the following code:
56 ```{r}
57 dir.folder<-dir() dir.folder<-dir.folder[1:22] for (j in
58 1:length(dir.folder)){
59     setwd(dir.folder[j])
60     file.copy("/spin1/users/kanferg/Images/Tax1bp_Shireen/per_well_Image/r
61 unn
62 .R",paste0("/spin1/users/kanferg/Images/Tax1bp_Shireen/per_well_Image/
63 ",d ir.folder[j]))
64     tifss<-dir()[grep(".tif$",dir())]
65     for (i in 1:length(tifss)){ name<-gsub(".tif",".txt",tifss[i])
66         file.create(name)
67     }
68     name.folder<-paste0(dir.folder[j]) #seq(1,length(tifss))
69     mydata<-
70     paste0("/spin1/users/kanferg/Images/Tax1bp_Shireen/per_well_Image/",na
71 me.folder)
72     #tifss<-dir()[grep(".tif$",dir())] sink(paste0(name.folder,".swarm"))
73     cat("#! /bin/bash")
74     cat("\n")
75     cat("#swarm -f first.swarm --module R/3.5")
76     cat("\n")
77     for (i in 1:length(tifss)){ name<-gsub(".tif",".txt",tifss[i])
78     cat("Rscript"," ",paste(mydata,"/runn",".R",sep =""),
79     ",paste(tifss[i])," ",paste(name)) cat("\n")
80 } sink()
81 setwd("../")
```

```
82 }
83 mydata<-"/data/kanferg/Ward_lab/Plate_4/" sink("second.swarm")
84 cat("#! /bin/bash")
85 cat("\n")
86 cat("#swarm -f second.swarm --module R/3.5") cat("\n")
87 for (i in 1000:1496){
88   name<-gsub(".tif",".txt",tifss[i])
89   cat("Rscript", " ",paste(mydata,"runn",".R",sep =""), "
90   ",paste(tifss[i]), " ",paste(name))
91   cat("\n") }
92 sink()
93
94 Segmented object number per well table are aggregated to a list
95 ```{r} HttQ23_1<-as.data.frame(list.observation$E02) HttQ23_2<-
96 as.data.frame(list.observation$F02) HttQ23_3<-
97 as.data.frame(list.observation$G02) HttQ103_1<-
98 as.data.frame(list.observation$E03) HttQ103_2<-
99 as.data.frame(list.observation$F03) HttQ103_3<-
100 as.data.frame(list.observation$G03)
101 HttQ23.tax_1<-as.data.frame(list.observation$E08) HttQ23.tax_2<-
102 as.data.frame(list.observation$F08) HttQ23.tax_3<-
103 as.data.frame(list.observation$G08) HttQ103.tax_1<-
104 as.data.frame(list.observation$E09) HttQ103.tax_2<-
105 as.data.frame(list.observation$F09) HttQ103.tax_3<-
106 as.data.frame(list.observation$G09)
107 vector.name<-
108 c("HttQ23_1","HttQ23_2","HttQ23_3""HttQ103_1","HttQ103_2","HttQ103_3",
109 "Ht
110 tQ23.tax_1","HttQ23.tax_2","HttQ23.tax_3","HttQ103.tax_1","HttQ103.tax
111 _2" ,"HttQ103.tax_3")
112 list.df<-
113 list(HttQ23_1,HttQ23_2,HttQ23_3HttQ103_1,HttQ103_2,HttQ103_3,HttQ23.ta
114 x_1
115 ,HttQ23.tax_2,HttQ23.tax_3HttQ103.tax_1,HttQ103.tax_2,HttQ103.tax_3)
116
117 Generate fitted curves using exponential decay model
118 ```{r} make.list<-function(input.list){
119 df.list<-as.data.frame(input.list) ls.temp<-list()
120 for (i in 1:16){
121 vec.cellnumber<-as.vector(t(df.list[i,1:15])) day<-1:15
122 df<-as.data.frame(cbind(day,vec.cellnumber)) colnames(df)<-
```

```
123 c("day","cellNumber") drc.plot<-try(drm(df$cellNumber~df$day,data =
124 df, fct =

125 EXD.3(),na.action = na.omit))
126 if (inherits(drc.plot,"try-error")){

127 next } else {

128 sl<-summary(drc.plot)
129 slope<-sl$coefficients[[3]]
130 slope.se<-sl$coefficients[[6]] pv.slope<-sl$coefficients[[9]]
131 ls.temp[[i]]<-as.data.frame(cbind(slope,slope.se,pv.slope))

132 } }

133 return(ls.temp)

134 } ```

135 Transformation of exponential decay fitted slope into ggplot2
136 compatible form

137 ```{r} drc.table<-function(input){

138 #browser() df.ctrl.drc<-as.data.frame(matrix(0,0,2))
139 colnames(df.ctrl.drc)<-c("day","cellNumber") colnames(input)<-c(1:38)
140 input<-input[,c(2:20)] mean.c<-median(input[,1])
141 li<-list(NULL) ctrl.temp<-rep(1,length(input[,1]))

142 li[[1]]<-ctrl.temp
143 for (i in 1:19){

144 ctrl.temp<-(input[,i])/mean.c

145 li[[paste0(i)]]<-ctrl.temp }

146 vec.num<-as.vector(li[[paste0(1)]]) vec.day<-rep(1,length(vec.num))
147 df.ctrl.drc<-cbind(vec.day,vec.num)

148 for (j in 1:19){ vec.num<-as.vector(li[[paste0(j)]]) vec.day<-
149 rep(j,length(vec.num)) df.ctrl.drc.temp<-cbind(vec.day,vec.num)
150 df.ctrl.drc<-rbind(df.ctrl.drc,df.ctrl.drc.temp)

151 }

152 df.ctrl.drc<-as.data.frame(df.ctrl.drc)

153 return(df.ctrl.drc)
154 }

155 ```
156 Eliminate Outliers Using Interquartile Range
```

```
157   ```{r}
158   l11103<-list()
159   for (i in 1:length(unique(drc.input.table.df$day))) {

160     d.temp<-filter(drc.input.table.df,day==i) outliers<-
161     scores(d.temp$survival_rate,type = c("iqr")) ind<-which(outliers == 0)
162     if (length(ind) > 0) {

163       d.temp<-d.temp[ind,]
164     }

165     l11103[[i]]<-mean(d.temp[,2]) }

166   ```
167   Preforming permutation analysis on the calculated slopes

168   ```{r} df.permut.tax<-
169   filter(df.anova.slope.pv,df.anova.slope.pv$name=="set1")
170   nrow(df.permut.tax)
171   #df.permut.tax<-df.permut.tax[1:32,] df.permut.notax<-
172   filter(df.anova.slope.pv,df.anova.slope.pv$name=="set2")
173   nrow(df.permut.tax)
174   #df.permut.notax<-df.permut.notax[1:32,]
175   # test intalisation
176   nsim<-10000 combine.df.slope<-
177   c(df.permut.notax$slope,df.permut.tax$slope) combine.df.name<-
178   c(df.permut.notax$name,df.permut.tax$name) dif.obse<-
179   mean(df.permut.notax$slope)-mean(df.permut.tax$slope) diffres<-
180   rep(NA,nsim)
181   for (i in 1:nsim){

182     sufffled.lables<-sample(combine.df.name, replace = F)

183     diffres[i]<-mean(combine.df.slope[sufffled.lables == "set1"]) -
184     mean(combine.df.slope[sufffled.lables == "set2"])
185   }

186   #calculate the two sided pvalue
187   pv<- length(diffres[abs(diffres) >= abs(dif.obse)])/nsim print(pv)
188
189
```

Supplementary Table S1

| Previously reported Lazarou et al. 2014 | | |
|---|---------|----------------|
| Name | Gene | Clone # |
| Single Knockout Lines | | |
| OPTN KO | OPTN | 24 |
| NDP52 KO | NDP52 | 5 |
| TAX1BP1 KO | TAX1BP1 | 3 |
| Triple Knockout Line | | |
| TKO | OPTN | 6, (parent 24) |
| | NDP52 | 6 |
| | TAX1BP1 | 6 |

| Name | Gene | Clone # | Exon Targeted | CRISPR sequence | Editing Results |
|------------------------------|-------------------------|---------|---------------|-----------------------------------|--|
| Single Knockout Lines | | | | | |
| p62 KO | p62 | 11 | 3 | GGCGCCTCCTGAGCACACGG | 1 1 basepair insertion 2 1 basepair deletion |
| Genotyping Primers | | | | | |
| Forward | ACAGTGACGACAGAGGGGA | | 270 | HpyCH4III cuts into 168, 99, 3 bp | |
| Reverse | AATGCGAGCTTGGTGTGCC | | | | |
| NBR1 KO | | | | | |
| NBR1 KO | NBR1 | 4 | 5 | GCCAGAGGATCCTGCAGTGC | 1 1 basepair insertion 2 19 basepair deletion 3 13 basepair deletion |
| Genotyping Primers | | | | | |
| Forward | ACCAACTGCAGATGCAAGTCC | | 249 | BtsI cuts into 175, 74 bp | |
| Reverse | AGAAACCTGTTTCAGCTTATTTA | | | | |